

1/21/05
TD-05-017

SQ01b Test Summary

Bernardo Bordini, Ruben Carcagno, Sandor Feher, Michael J. Lamm, Darryl Orris, Yrij Pischalnikov,
Cosmore Sylvester, Michael Tartaglia, Alexander V. Zlobin
FNAL

Scott E. Bartlett, Shlomo Caspi, Daniel R. Dietderich, Paolo Ferracin, Steve A. Gourlay, Charles R.
Hannaford, Aurelio R. Hafalia, Alan F. Lietzke, Sara Mattafirri, Alfred D. McInturff, Gianluca Sabbi
LBNL

Content:

1. Introduction.....	2
2. Quench history.....	2
3. Ramp rate dependence.....	6
4. Temperature dependence.....	7
5. AC Loss measurements.....	8
6. Magnetic measurements.....	9
7. Strain Gauge Measurements.....	33

1. Introduction

SQ01b was built at LBNL. It was shipped to Fermilab in November of 2004. The magnet was interfaced to VMTF dewar in December 2004. Final electrical checkout was completed on January 11th, 2005 and the following two days warm magnetic measurements took place. The magnet was cooled down to 4.5 K on January 14th, 2005 and after cold check out was completed the magnet had been floated for three days during the long weekend. The test was resumed on January 18th, 2005. After four days of testing the test was completed on January 21st, 2005.

2. Quench history

The initial goal of the test was to train the magnet at 4.5K with the default ramp rate cycle. This cycle was developed at LBL: between 0A-5000A a 40A/s ramp rate was used. Then the ramp rate was changed to 20A/s between 5000A – 8000A. At the last cycle, from 8000A to quench the magnet was ramped with 8A/s ramp rate. The first quench of the magnet was at 10750 A. This quench current was comparable with the quench current observed at LBL. On the other hand after quenching the magnet ten times it still didn't exhibited significant improvements. The highest quench current achieved was at 11028A and the lowest was at 9919A. The rest of the quenches were in between these quench current values distributed erratically. The conclusion was that the magnet quench current already reached its plateau value so we can move onto the next step in the program.

Ramp rate dependence studies were short since the magnet quench current ramp rate dependence was quite flat. To increase the sensitivity of the measurement the magnet was quenched at 500 A/s. The quench current only dropped to 6884 A. This low ramp rate dependence was confirmed with AC loss measurements at later part of the test program (see AC loss measurement section).

The magnet was cooled down to 2.2K. Training of the magnet at 2.2K was short. Practically we didn't observe any increase of the quench current. The highest quench current was at 11143A. The magnet quench behavior was quite stable. So after six quenches we increased the temperature back to 4.5K and quenched the magnet couple of times. As it was expected the magnet quench current didn't improve, it was still at the same current level – within the ~1000 A band - as it was prior to cooling it down to 2.2K.

After AC loss measurements we decided to perform few quenches at different temperatures. Prior to some of the quenches we also cycled the magnet with different ramp rates between 5A-6500A five times. The maximum current 11644A was achieved at 3.0K. There was no evidence of quench current dependence with or without ramp cycles performed prior to quenching the magnet.

Table 1 and Fig 1. summarize the quench history of SQ01b. Table I also contains the quench locations in notations used at MTF.

SQ01b Quench History

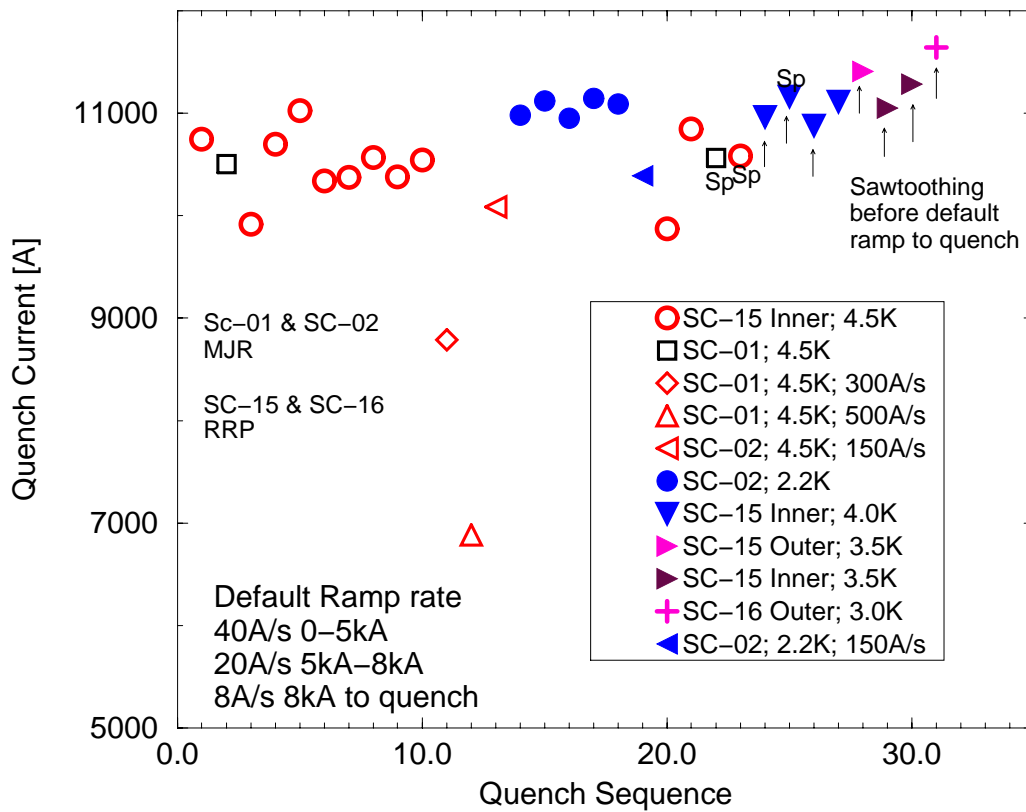


Fig. 1 Quench history of SQ01b. Little arrows underneath of the symbols mark those quenches which were performed after cycling the magnet five times between 0A-6500A with different ramp rates (40A/s, 100A/s, 300A/s).

Table I.

File	Curren t (A)	dI/dt (A/sec)	MIITs	QDC	1st VTseg	CgDeMaBot	Comments
sq01.Quench.050118153659.184	1007	0	0.17	WcoilGnd	QC_B_QC_Y	4.453	1000A manual trip
sq01.Quench.050118175838.957	1005	0	0.09	WcoilGnd	QP3_2_QP02_1	4.453	1000A manual trip
sq01.Quench.050118181041.726	1718	7	0.87	HcoilHcoil	QO3_2_QO02_1	4.452	lead trip
sq01.Quench.050118184155.516	3000	0	1.33	HcoilHcoil	QP05_2_QP04_2	4.454	3000A, spot heater induced quench
sq01.Quench.050118193844.641	10613	6	0.81	WcoilIdot	QC_B_QC_Y	4.455	6988A, DQD coil SI leads
sq01.Quench.050118195827.256	7359	0	0.81	WcoilIdot	QP3_2_QP02_1	4.460	7000A, trip due to DQD SI Wcoil
sq01.Quench.050118203455.309	10750	8	4.28	HcoilHcoil	QO07_2_QO06_2	4.463	1st quench, 10750A, 8A/sec
sq01.Quench.050119105734.365	10505	8	4.42	HcoilHcoil	QP_B_QP_Y	4.462	2nd quench, 10505A, 8A/sec, 4.5K
sq01.Quench.050119114220.263	9919	8	4.19	HcoilHcoil	QO07_2_QO06_2	4.466	3rd quench, 8A/sec, 4.5K, Iq=9919A
sq01.Quench.050119122329.388	10696	8	2.87	HcoilHcoil	QO07_2_QO06_2	4.469	4th quench, 8A/sec, 4.5K, Iq=10696A
sq01.Quench.050119140220.068	11028	7	4.00	HcoilHcoil	QO07_2_QO06_2	4.464	5th quench, 8A/sec, Iq=11028A, 4.5K
sq01.Quench.050119142051.289	10339	7	4.37	HcoilHcoil	QO07_2_QO06_2	4.487	I=10339A, 8A/s, 4.5K, 6th quench
sq01.Quench.050119144414.174	10374	7	4.31	HcoilHcoil	QO07_2_QO06_2	4.480	7th quench, Iq=10374A, 8A/s, 4.5K
sq01.Quench.050119150703.918	10568	7	4.31	HcoilHcoil	QO07_2_QO06_2	4.484	8th, Iq=10568, 8A/s, 4.5K
sq01.Quench.050119153035.513	10378	7	4.37	HcoilHcoil	QO07_2_QO06_2	4.489	9th quench, Iq=10378A, 8A/s, 4.5K
sq01.Quench.050119161955.273	10543	7	4.29	HcoilHcoil	QO07_2_QO06_2	4.487	10th quench, 8A/s, 4.5K, Iq=10543A
sq01.Quench.050119163224.010	8790	301	2.17	HcoilHcoil	QP_B_QP_Y	4.507	11th quench, Iq=8790A, 300A/s, 4.5K
sq01.Quench.050119165528.015	6884	502	1.76	HcoilHcoil	QP_B_QP_Y	4.495	12th quench, 500A/sec, 4.5K, Iq=6884A
sq01.Quench.050119170749.572	10084	150	2.88	WcoilGnd	QC_B_QC_Y	4.493	13th quench, 150A/s, 4.5K, Iq=10084.5A
sq01.Quench.050119203331.905	10982	8	2.45	HcoilHcoil	QC_B_QC_Y	2.156	14th, Iq=10982A, 8A/s, 2.2K
sq01.Quench.050119210036.092	11120	8	2.93	HcoilHcoil	QC_B_QC_Y	2.158	15th, 2.2K, 8A/sec, Iq=11120A
sq01.Quench.050119212626.838	10954	7	2.47	HcoilHcoil	QC_B_QC_Y	2.156	16th quench, 8A/sec, 2.2K, Iq=10954A
sq01.Quench.050119215054.053	11143	7	2.46	HcoilHcoil	QC_B_QC_Y	2.154	17th Quench, 8A/sec, 2.2K, Iq=11143A
sq01.Quench.050119221242.036	11092	7	2.47	HcoilHcoil	QC_B_QC_Y	2.155	18th quench, 8A/sec, 2.2K, Iq=11092A
sq01.Quench.050119222220.661	10389	150	2.33	HcoilHcoil	QC_B_QC_Y	2.169	19th quench, 150A/s, 2.2K, Iq=10389A
sq01.Quench.050120090536.252	9872	8	4.29	HcoilHcoil	QO07_2_QO06_2	4.479	20th quench, 4.5K, 8A/s, Iq=9879A
sq01.Quench.050120092941.286	10845	8	4.12	HcoilHcoil	QO07_2_QO06_2	4.491	21st quench, 8A/s, 4.5K, Iq=10845A

sq01.Quench.050120103701.197	2658	75	0.38	HcoilHcoil	QP01_1_QC_G	4.490	Trip while performing energy loss measurement @75A/sec
sq01.Quench.050121103122.832	10565	8	4.72	HcoilHcoil	QP_Y_QP_R	4.491	22nd quench, 8A/s, 4.5K, Iq=10565A
sq01.Quench.050121110118.351	10584	8	6.08	HcoilHcoil	QO07_2_QO06_2	4.504	Iq=10584A, 8A/sec, 4.5K, 23rd quench
sq01.Quench.050121122137.200	10966	7	3.43	HcoilHcoil	QO07_2_QO06_2	3.987	24th quench, 8A/s, 4.0K, Iq=10966A
sq01.Quench.050121130059.694	11165	8	3.89	HcoilHcoil	QO07_2_QO06_2	3.828	25th quench, 8A/s, 4.0K, Iq=11165A
sq01.Quench.050121140459.723	10880	8	3.11	HcoilHcoil	QO07_2_QO06_2	4.003	26th quench, Iq=10880A, 4.0K, 8A/s
sq01.Quench.050121152105.138	11115	7	3.48	HcoilHcoil	QO07_2_QO06_2	3.986	27th quench, Iq=11115A, 8a/s, 4.0K
sq01.Quench.050121173630.161	11408	8	2.42	HcoilHcoil	QO04_2_QO03_2	3.504	28th quench, 8A/s, Iq=11408A, 3.5K
sq01.Quench.050121184211.000	11051	8	2.96	HcoilHcoil	QO07_2_QO06_2	3.412	also QO03_2_QO02_2 started <.2msec
sq01.Quench.050121193853.414	11284	8	2.91	HcoilHcoil	QO07_2_QO06_2	3.455	Quench # 29, Iq=11051 A, 8 A/s
sq01.Quench.050121214354.598	11644	8	2.42	HcoilHcoil	QP04_2_QP03_2	2.900	Quench # 30, Iq=11284 A, ramp = 8 A/s
							31st quench, 8A/s, Iq=11644A, 3.0K
							also QO03_2_QO02_2 started <.2msec

QO07_2_QO06_2 is a coil labeled at LBL as SC-15
 QP_B_QP_Y is a coil labeled at LBL as SC-01
 QC_B_QC_Y is a coil labeled at LBL as SC-02
 QP_Y_QP_R is a coil labeled at LBL as Nb3Sn Splice between SC-01 and another NbTi splice
 QP04_2_QP03_2 is a coil labeled at LBL as SC Inner L2

3. Ramp Rate Dependence

Ramp rate dependence studies started at 300A/s. Since the quench current was relatively high to see more clearly the ramp rate dependence the ramp rate was increased to 500A/s. The last quench current value we took was at 150A/s. There was no need to decrease the ramp rate further since already the quench current was at the “quench current band” level observed at 8A/s ramp rate quenches. On the other hand the ramp rate dependence suggests that the magnet is likely to be quite close to its critical current value.

SQ01B

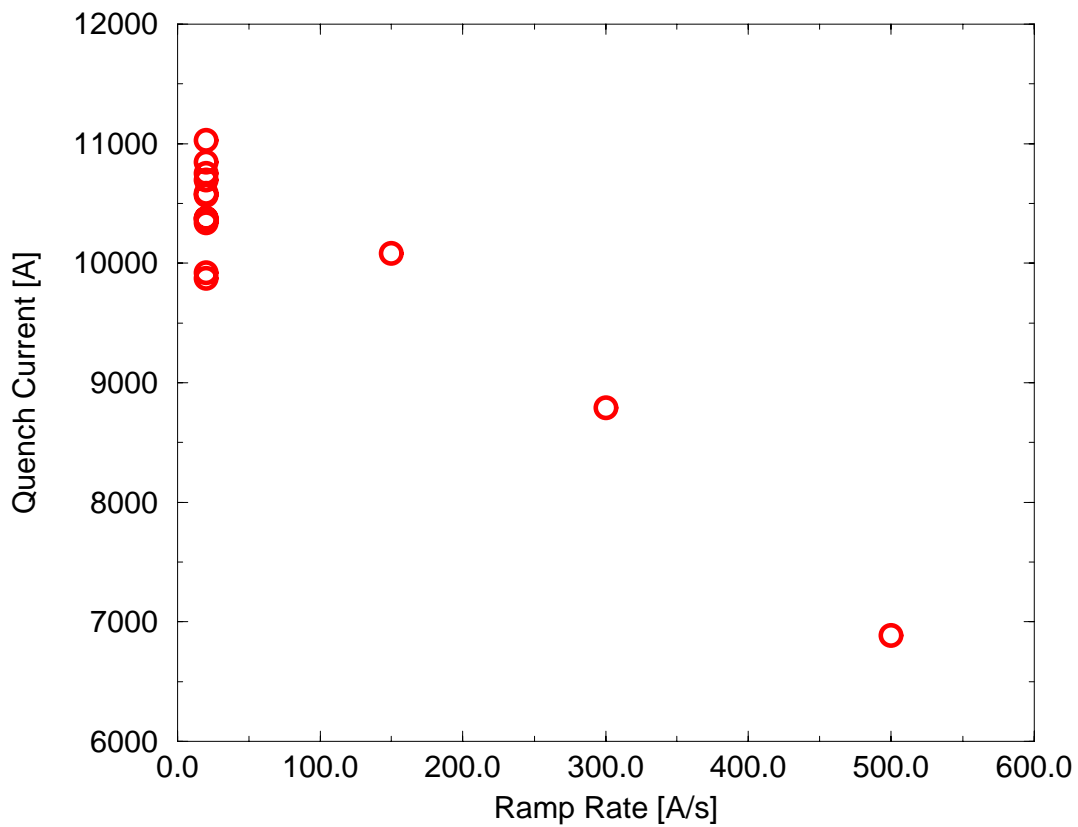


Fig 2. Quench current ramp rate dependence.

4. Temperature Dependence Studies

After training the magnet at 2.2 K liquid helium bath temperature and observing that no quench current increase there was practically no point to perform temperature dependence studies. However, we also observed that the magnet quench locations at 4.5K were at the coil wound from RRP conductor and quenches at 2.2 K were in the coil wound from MJR conductor. We tried to investigate at what temperature the quenches move from the RRP coil to the MJR coil. From Fig. 3 we can conclude that up 3 K the quenches occur in the RRP coil. Although the quenches are erratic the quench current (RRP coil) is gradually increasing. Once the quenches appear in MJR coil the quench current drops a bit.

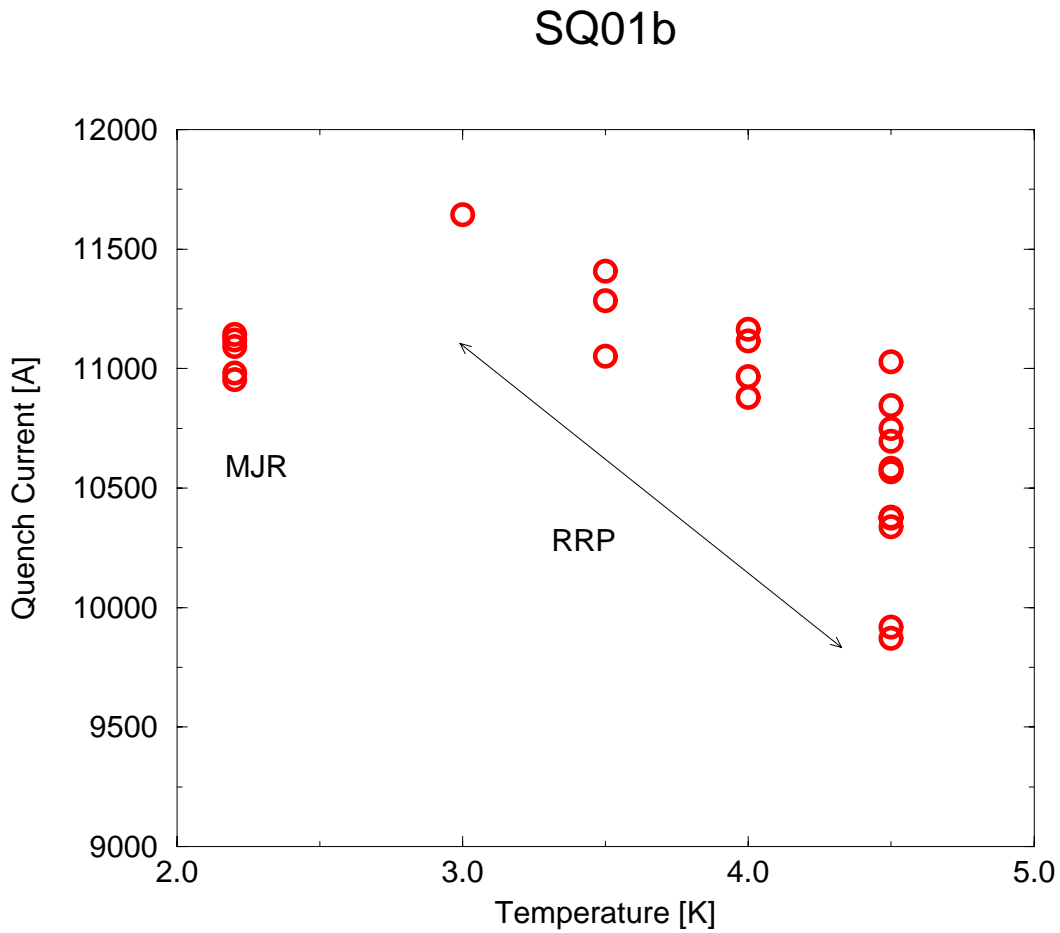


Fig. 3. Temperature dependence.

5. AC loss measurements

Energy Loss measurements were performed on SQ01b at 4.5K using two HP3458A Digital Multimeters (dmm) setup to integrate over 1 power line cycle and sample at 60Hz. One dmm measured the magnet voltage and the second dmm measured the magnet current via the power system current transductor. The magnet was ramped between 500A and 6500A for all measurements. Five measurements were performed at each ramp rate from 100A/se to 500A/s in steps of 50A/s; three pre-ramp cycles were performed before each new ramp rate.

- Measured hysteresis = 540 \pm 25 Joules
- Measured slope = 0.21 \pm 0.08J/A/s

The following is a plot of the data:

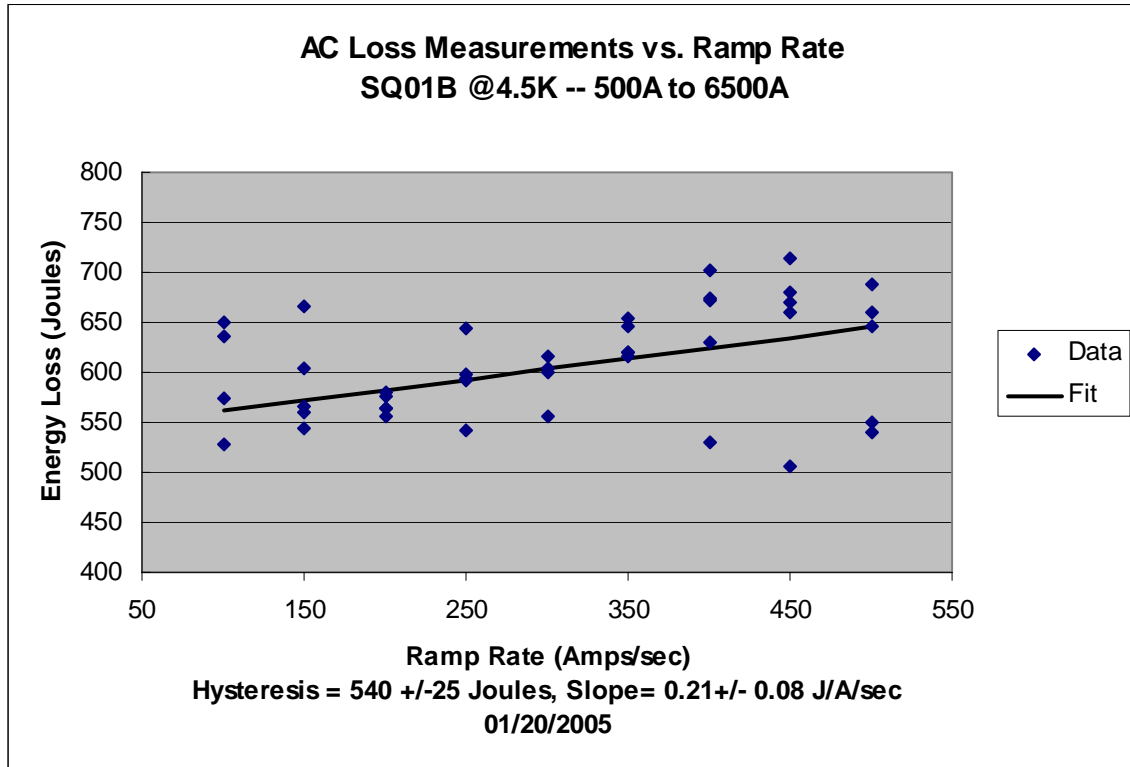


Fig. 4. AC loss measurement plot as a function of current ramp rate.

Table 2.

**SQ01B Energy Loss Measurement Summary @4.5K --
500Amps to 6500Amps**

<i>Ramp Rate(Amps/sec)</i>	<i>Energy Loss(Joules)</i>	<i>Integral Volts</i>
100	527.295471	-0.000199
100	574.087952	0.02991
100	650.41217	0.045231
100	635.929749	0.057873
100	357.863525	-0.019617
150	666.714172	0.046922
150	566.627686	0.017699
150	543.439575	0.007706
150	559.98291	0.003288
150	603.147339	-0.000155
200	564.733093	0.004016
200	555.55011	-0.003003
200	580.63324	-0.01225
200	563.956482	0.013738
200	576.17865	-0.007278
250	591.44635	0.012407
250	597.721375	0.009828
250	594.654602	0.007403
250	643.483398	0.012726
250	542.826721	-0.007368
300	556.432617	-0.00104
300	604.172607	0.003618
300	616.014099	0.005545
300	600.608154	0.008199
350	620.638794	0.019037
350	615.122986	0.007857
350	620.107483	0.009071
350	645.731079	-0.000721
350	653.134338	0.029152
400	671.182983	-0.005458
400	702.361267	0.023685
400	529.208374	-0.020258
400	674.666443	0.006783
400	630.68396	0.015069
450	714.877808	0.030977
450	659.836609	0.009291
450	506.691803	-0.025948
450	669.841125	0.008818
450	680.633606	0.016899
500	687.085815	0.005949
500	539.163086	-0.021947
500	549.721191	-0.010025
500	646.432068	0.007947
500	659.757141	0.010364

Magnetic measurements

Measurements of magnetic fields in the aperture were performed before and after cooling down. The measurement system was set up above VMTF cryostat and utilized 250 mm long probe (active length), 25 mm in diameter. The probe had a tangential winding for measurement of high order harmonics as well as dedicated dipole and quadrupole windings for measurement of low order harmonics. Voltages generated in the windings during the probe rotation were sampled and read 128 times per rotation using HP3458 DVMs. An additional DVM was used to monitor the magnet current. DVMs were triggered simultaneously by an angular encoder on the probe shaft, synchronizing measurements of the field and current. For all measurement analyses the probe was centered in the transverse plane using the feed down from quadrupole to dipole and the coordinate system was oriented such that the skew quadrupole is zero. The harmonic are presented at the reference radius of 1 cm in the coordinate system with Z-axis pointing from the return to the lead end (negative axes pointing toward the return end while the positive axes pointing toward the lead end) and normalized by the main field component at the magnet center ($Z=0$).

Warm Z-scan

During the warm measurements the magnet was energized at a room temperature by a small (2 A) current that reversed sign at every probe axial position in order to cancel fields not related to the magnet current. Figure 5 presents the transfer function and Figures 6-9 show low and high order harmonics as functions of the probe center coordinate.

Cold Z-scans

The cold Z-scans were performed at 4.2 K with 125 mm steps in axial direction at 4000 A, 7000 A and 9000 A currents during the ramp up. Figure 10 presents the transfer function and Figures 11-18 show low order harmonics as functions of the probe center coordinate.

Loops

During the loop measurements, the current was ramped up to 9000 A in two consecutive cycles with 10 A/s ramp rate. The probe was centered in the magnet at $Z=0$. Figure 19 presents the transfer function and Figures 20-27 show low order harmonics as functions of the magnet current in the first and second cycles.

Stairstep measurement

The current was gradually raised up to 9000 A with the ramp rate of 20 A/s and 2 minute dwells upon 1000 A, 2000 A, 4000 A, 6000 A, 8000 A and 9000 A currents at the ramps up and down. The current profile is presented in Figure 24 and the low order harmonics are shown in the Figures 29-36 as functions of time.

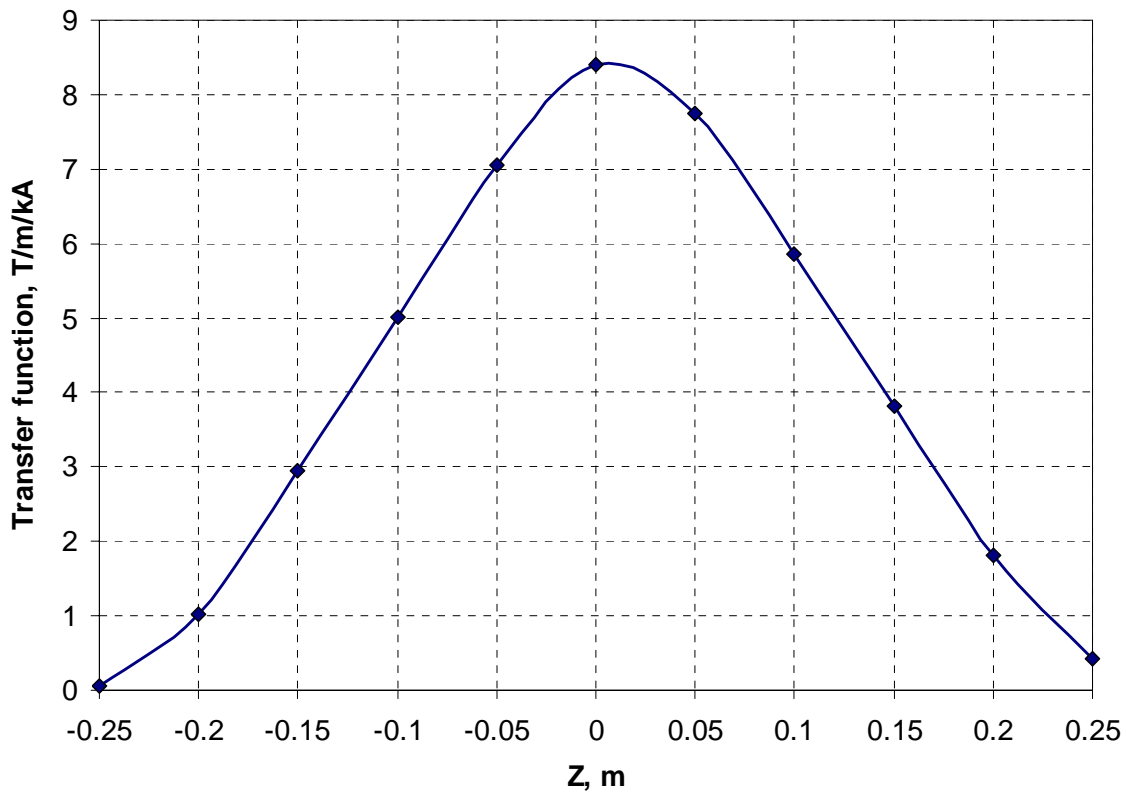


Figure 5. Transfer function as a function of axial coordinate.

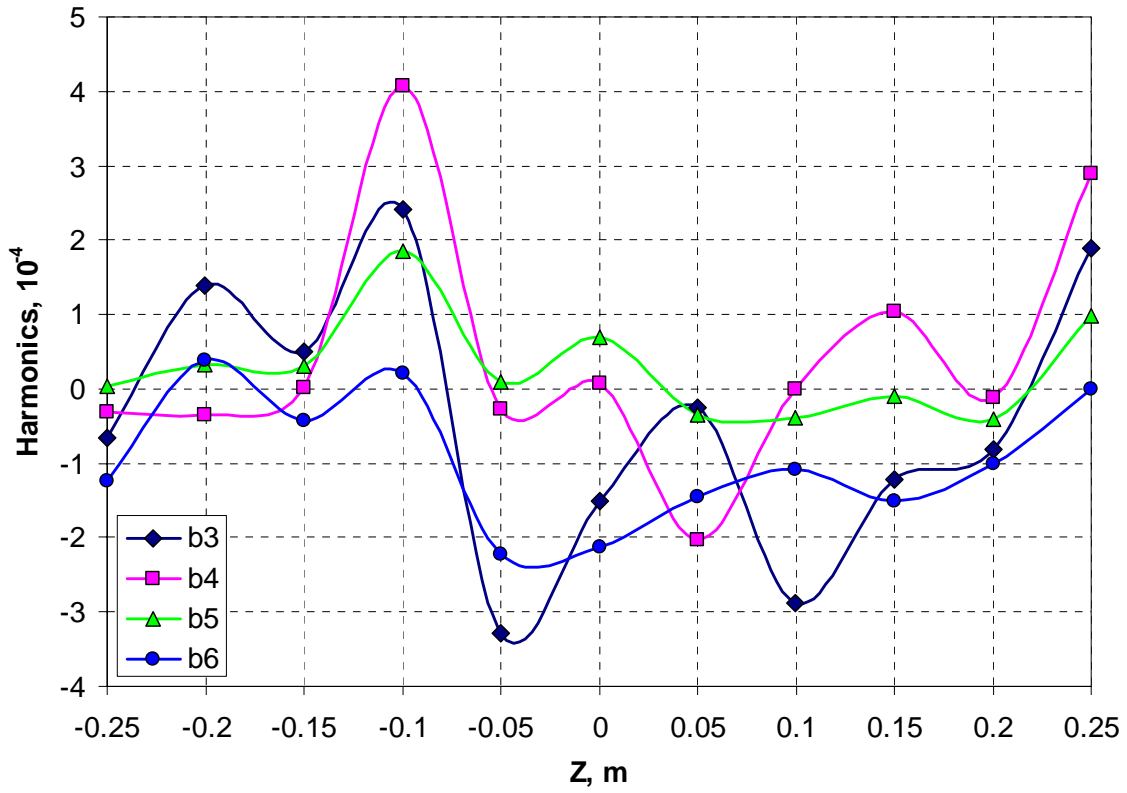


Figure 6. Low order normal harmonics as functions of axial coordinate.

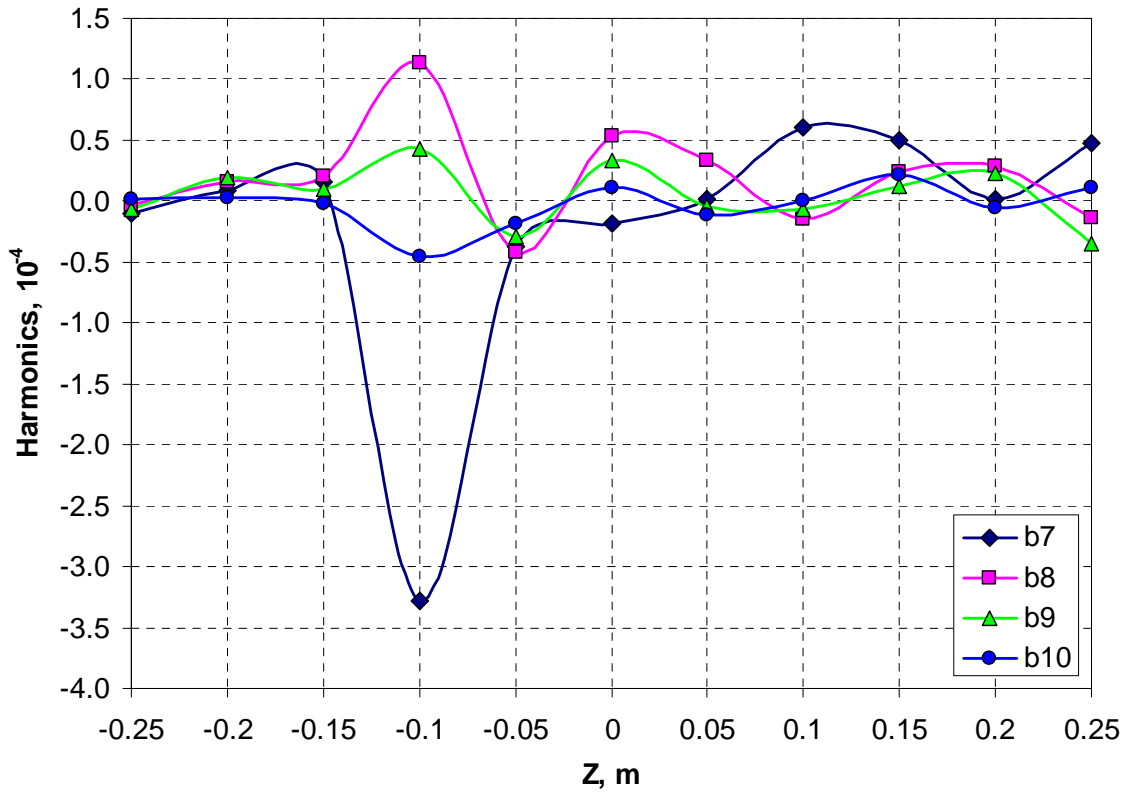


Figure 7. High order normal harmonics as functions of axial coordinate.

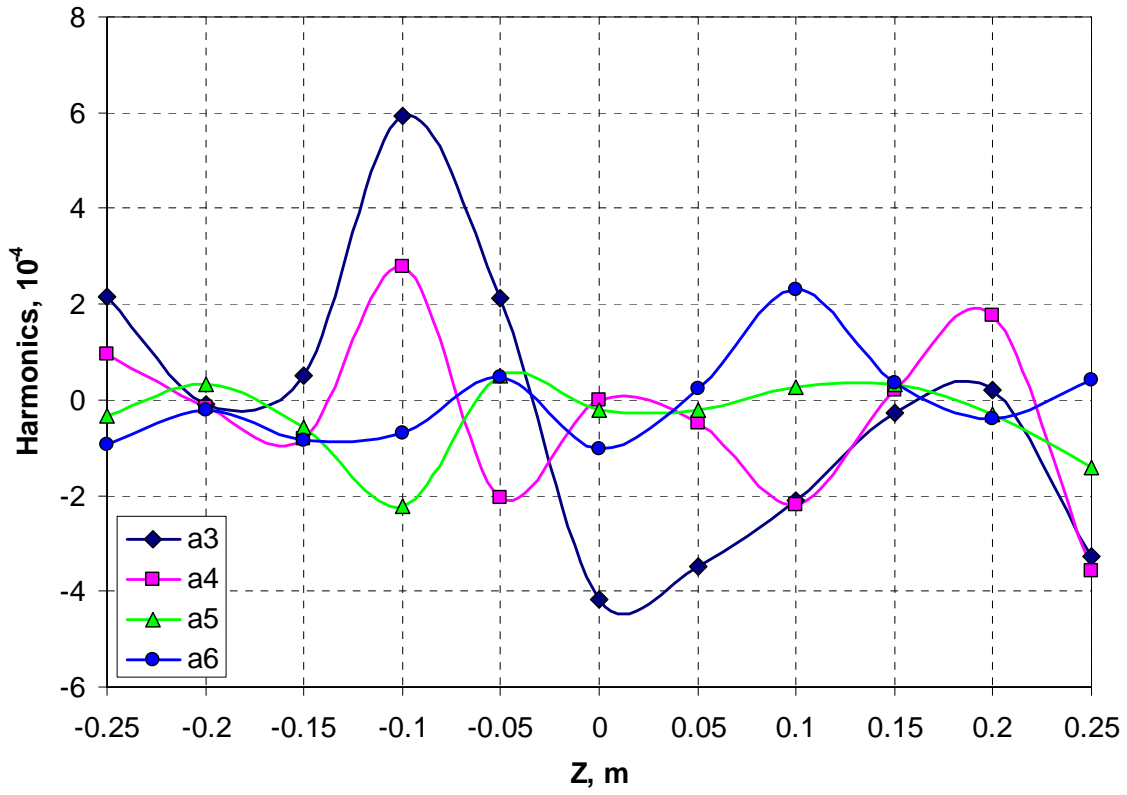


Figure 8. Low order skew harmonics as functions of axial coordinate.

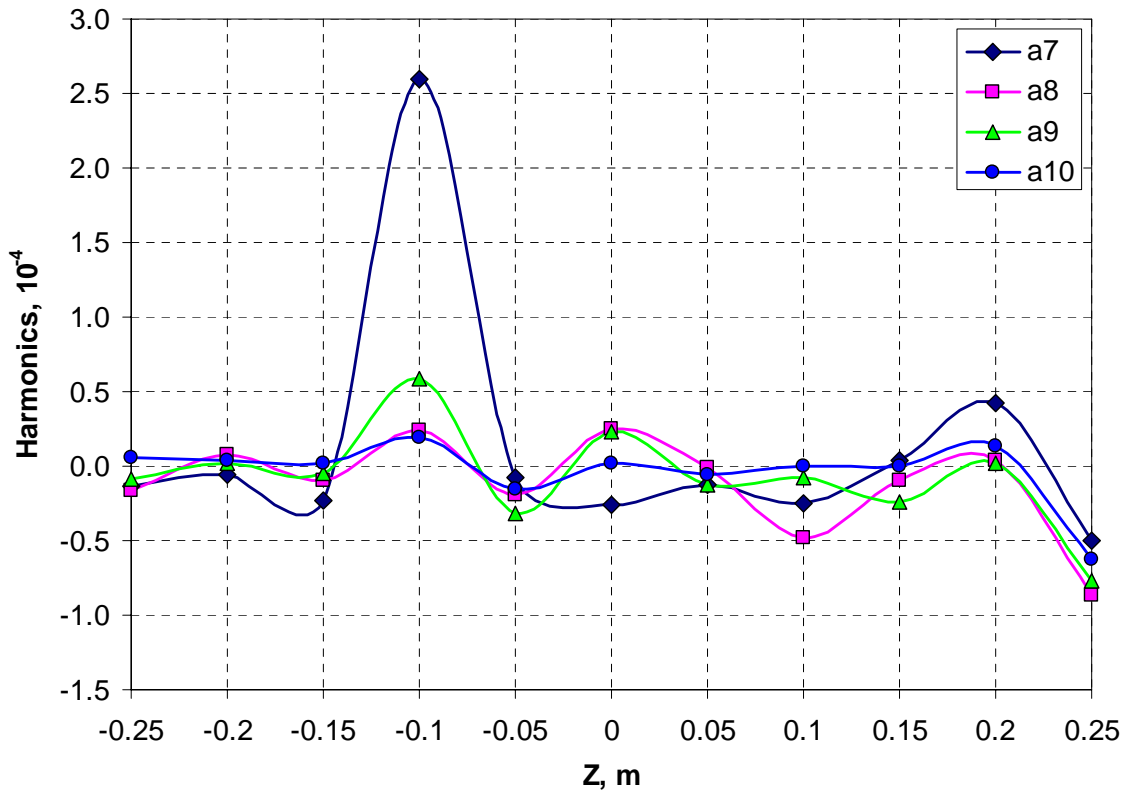


Figure 9. High order skew harmonics as functions of axial coordinate.

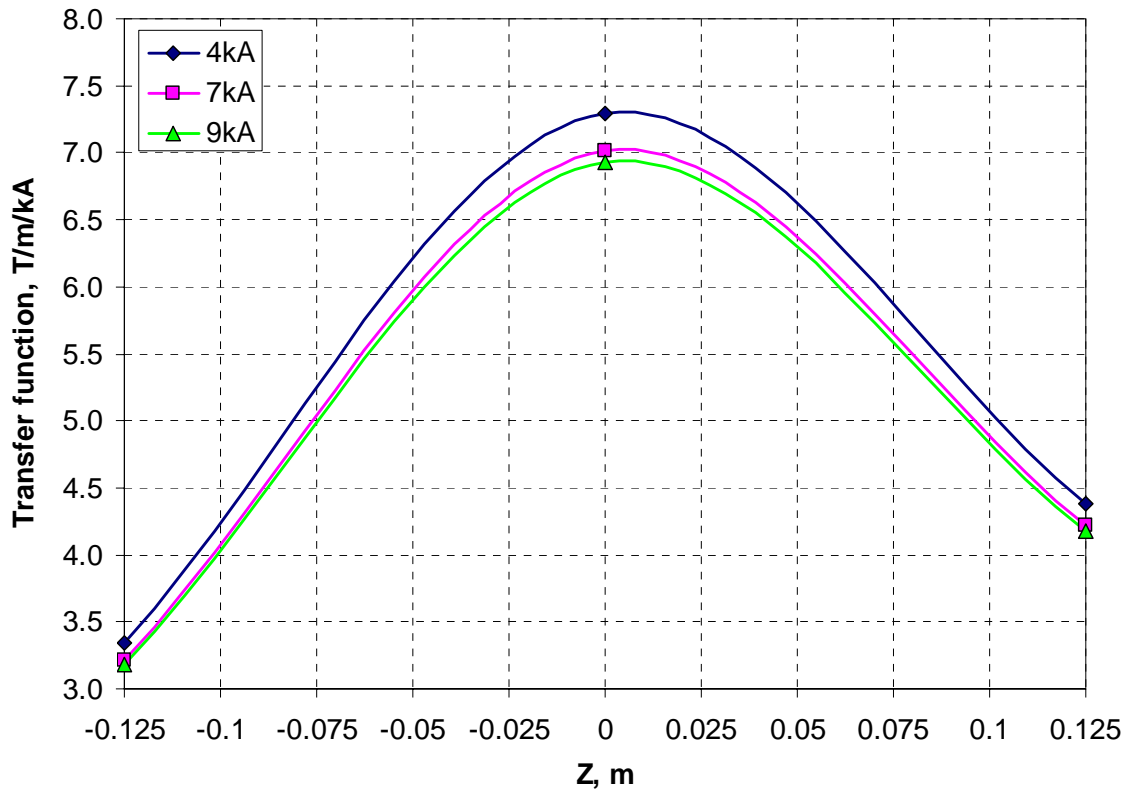


Figure 10. Transfer function as a function of axial coordinate.

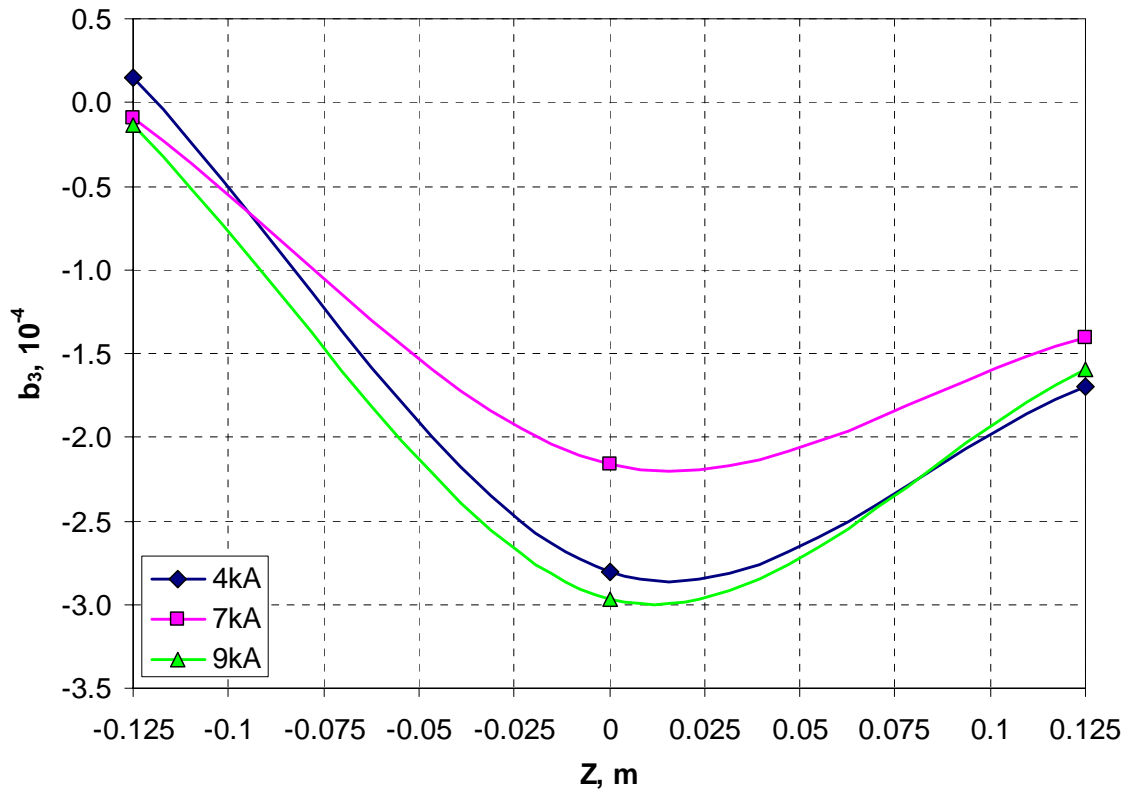


Figure 11. Normal sextupole as a function of axial coordinate.

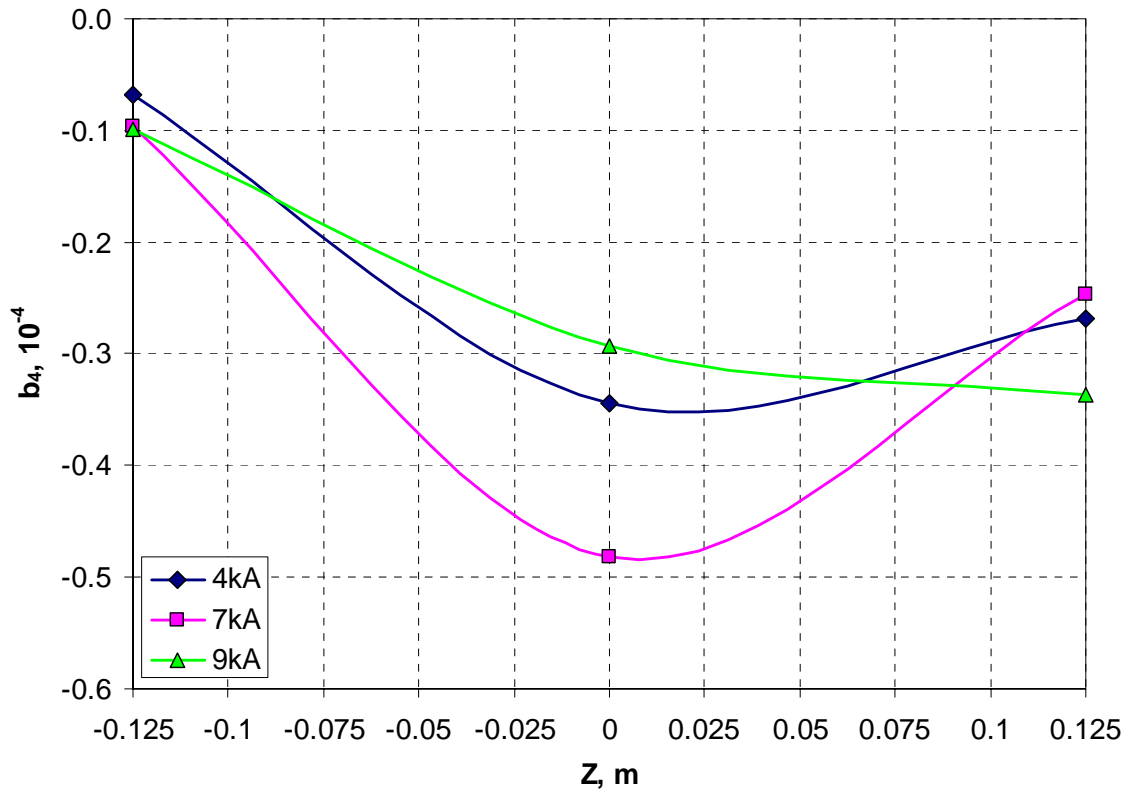


Figure 12. Normal octupole as a function of axial coordinate.

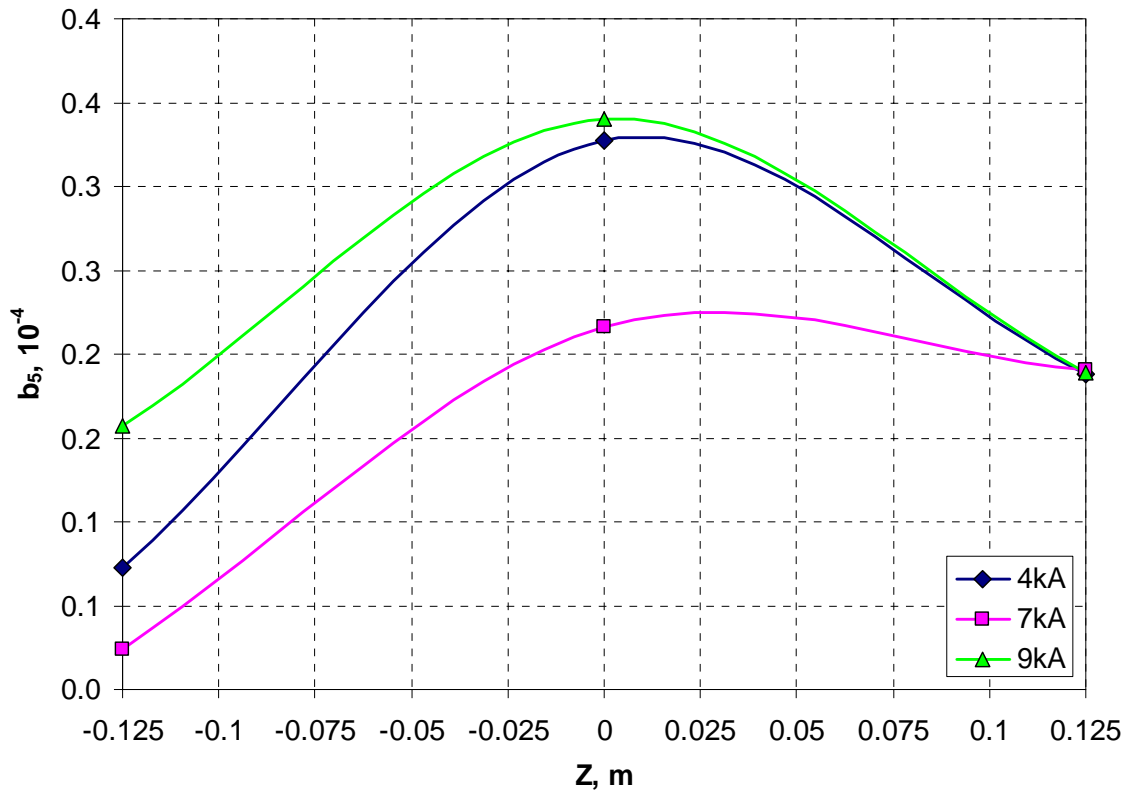


Figure 13. Normal decapole as a function of axial coordinate.

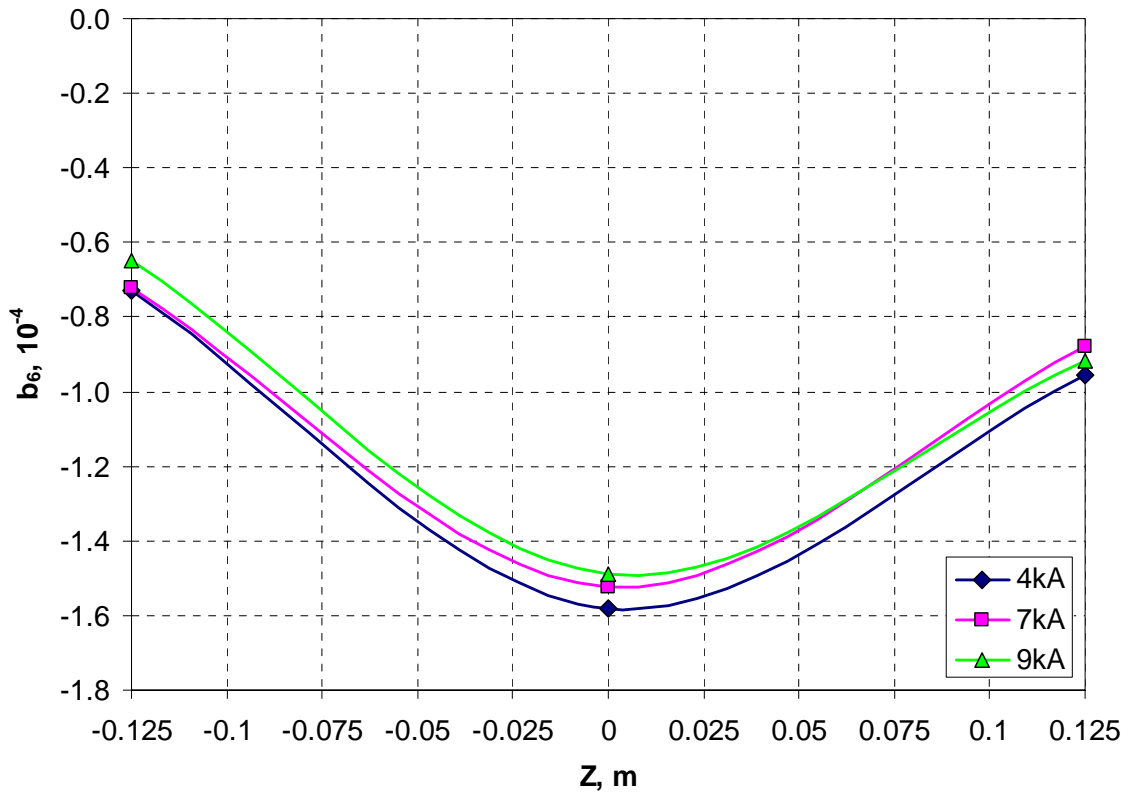


Figure 14. Normal dodecapole as a function of axial coordinate.

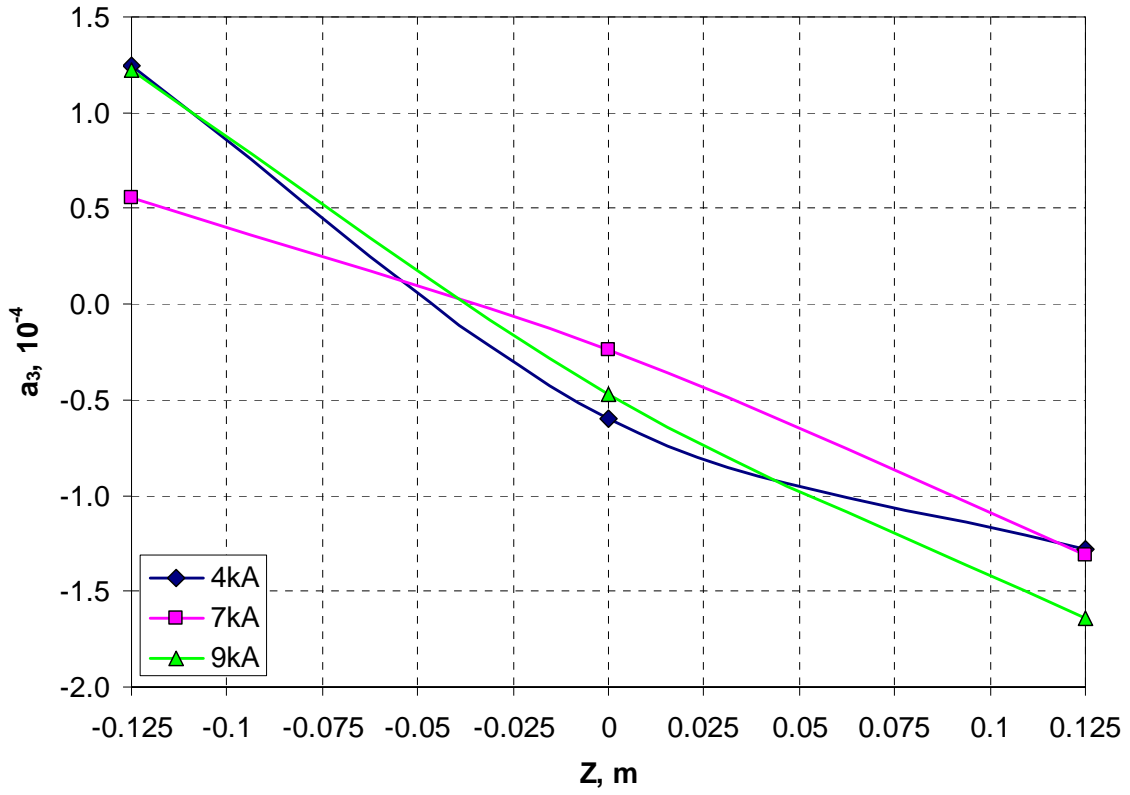


Figure 15. Skew sextupole as a function of axial coordinate.

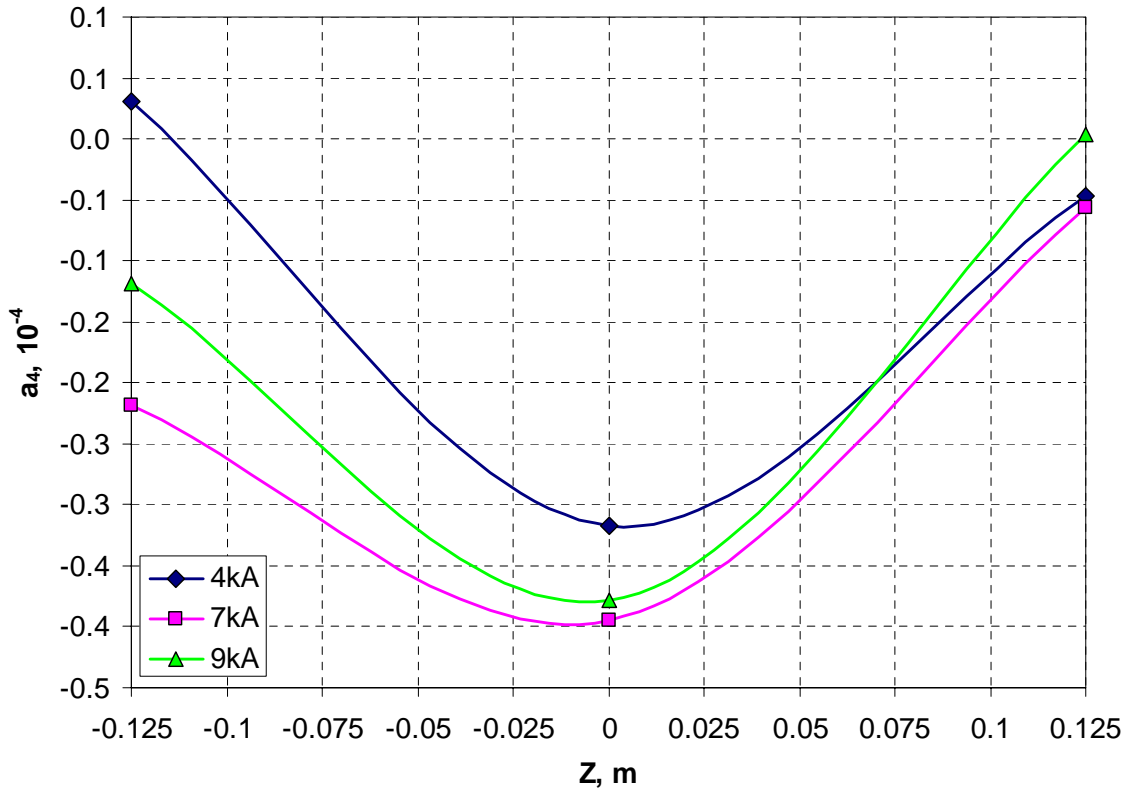


Figure 16. Skew octupole as a function of axial coordinate.

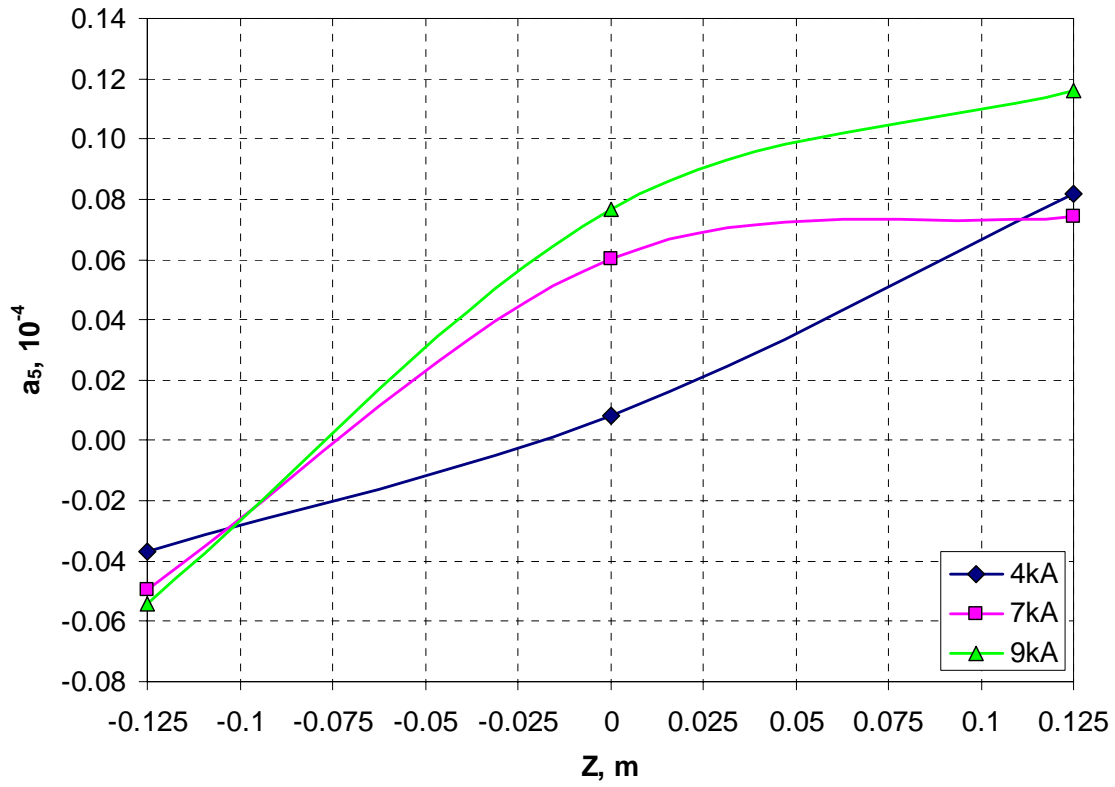


Figure 17. Skew decapole as a function of axial coordinate.

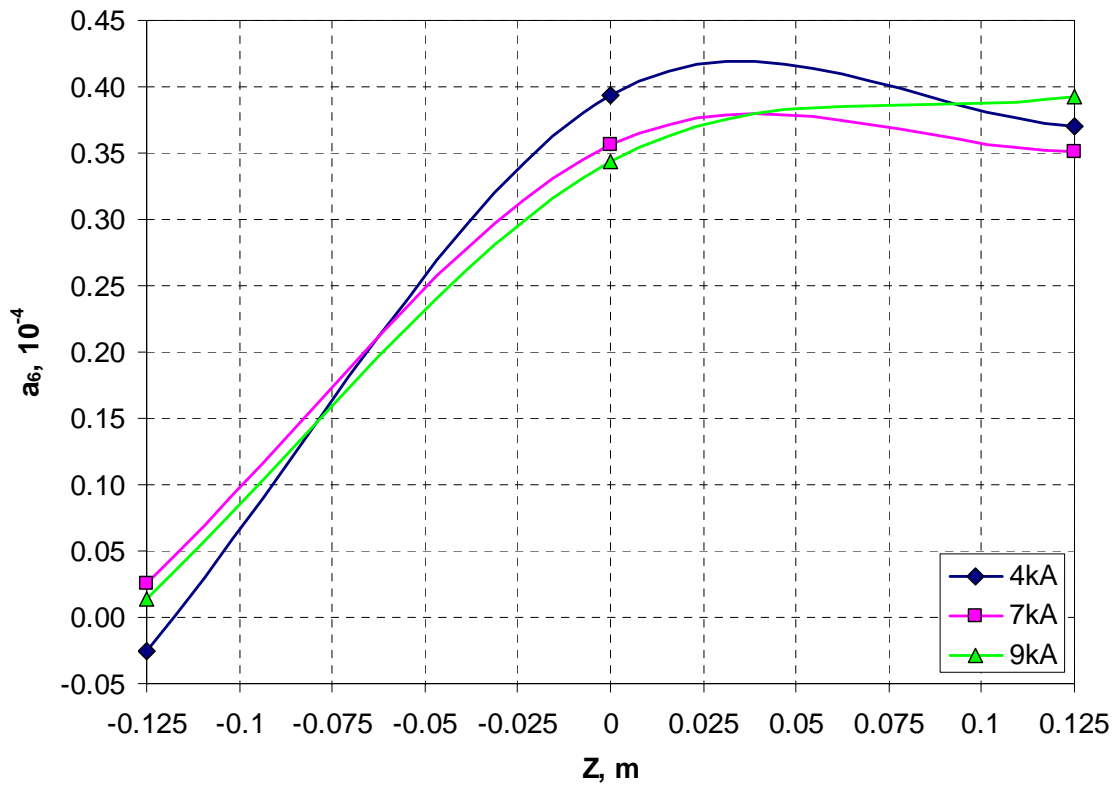


Figure 18. Skew dodecapole as a function of axial coordinate.

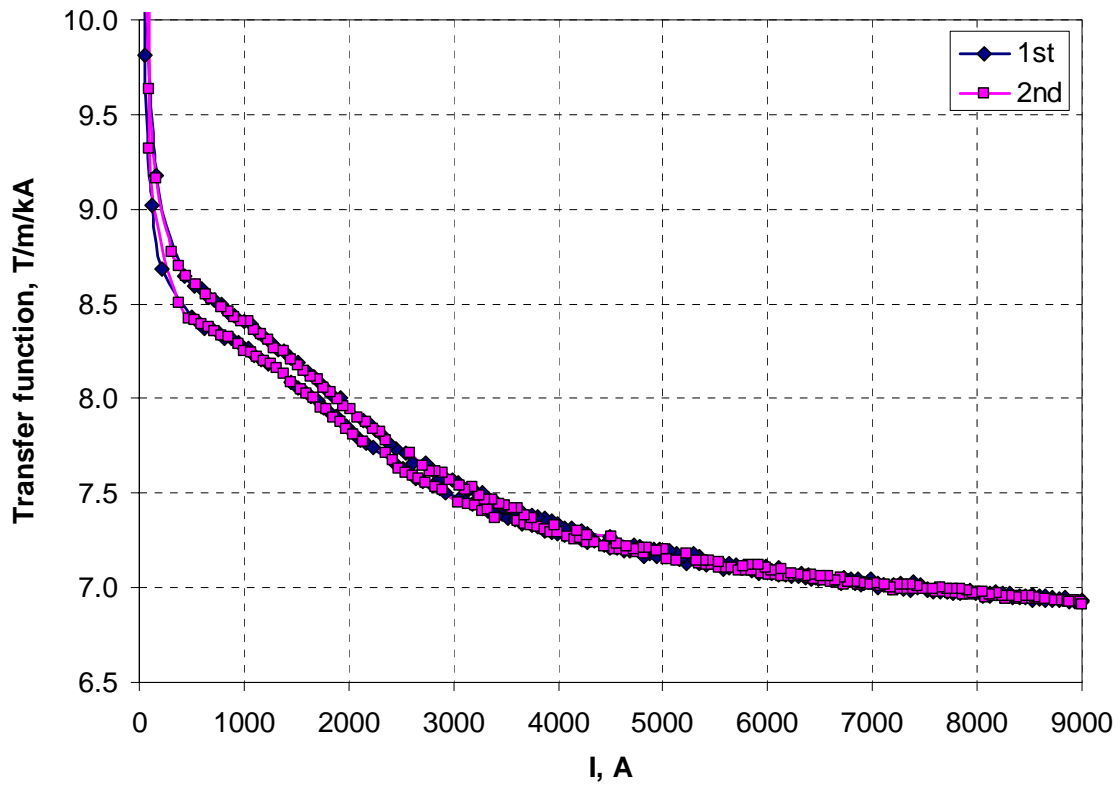


Figure 19. Transfer function as a function of current.

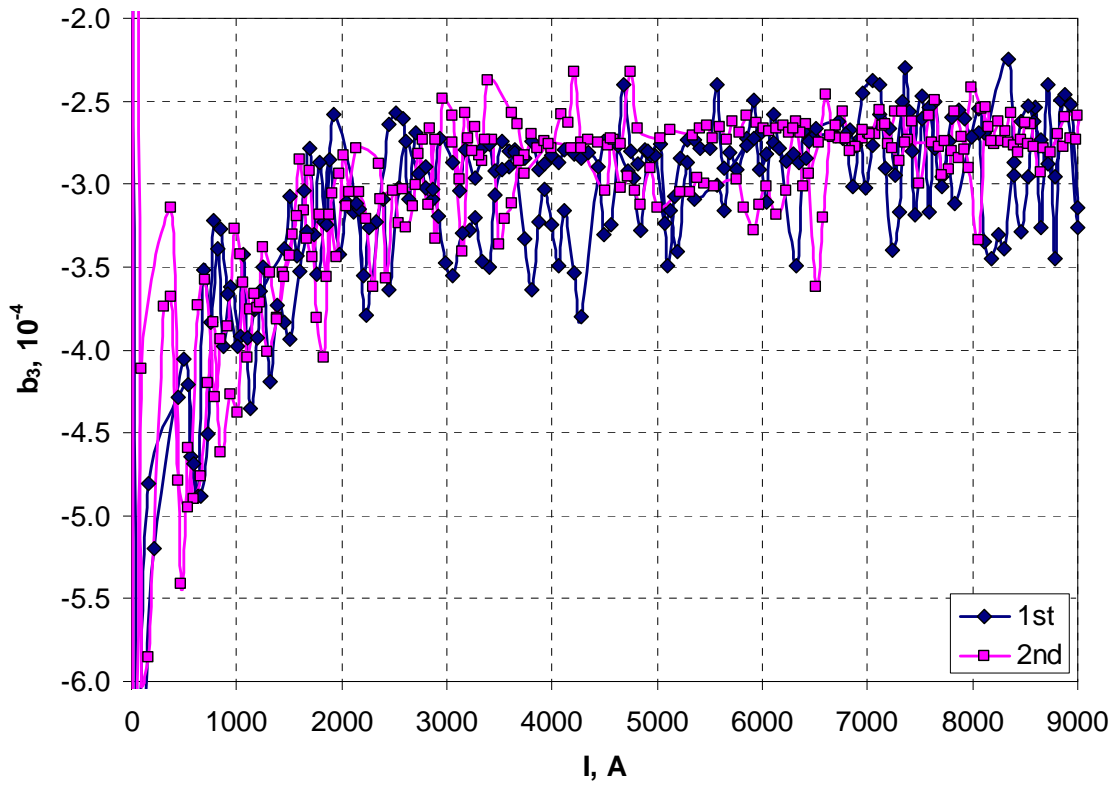


Figure 20. Normal sextupole as a function of current.

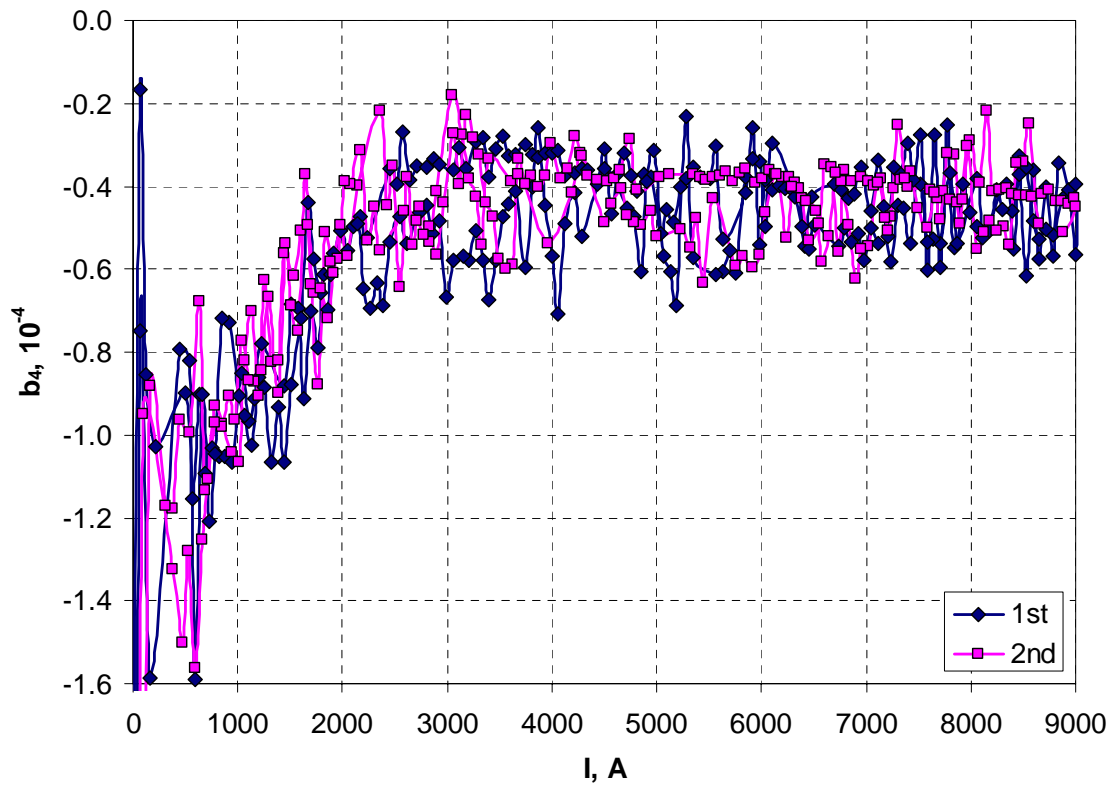


Figure 21. Normal octupole as a function of current.

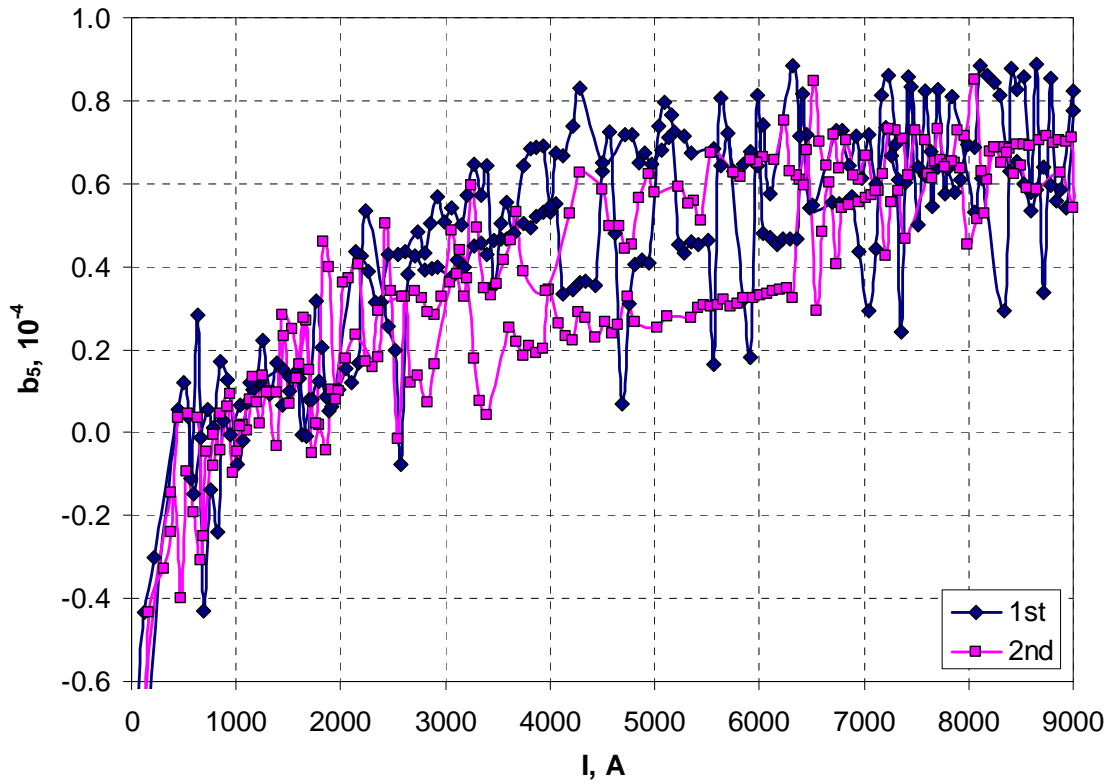


Figure 22. Normal decapole as a function of current.

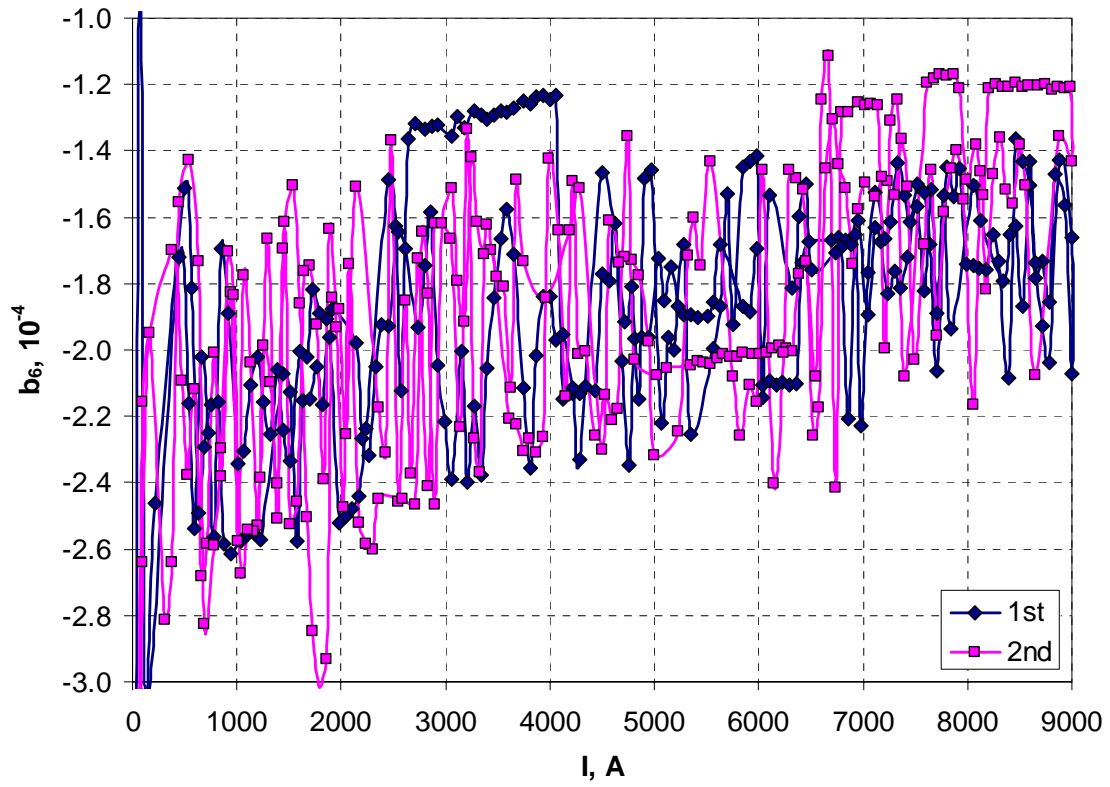


Figure 23. Normal dodecapole as a function of current.

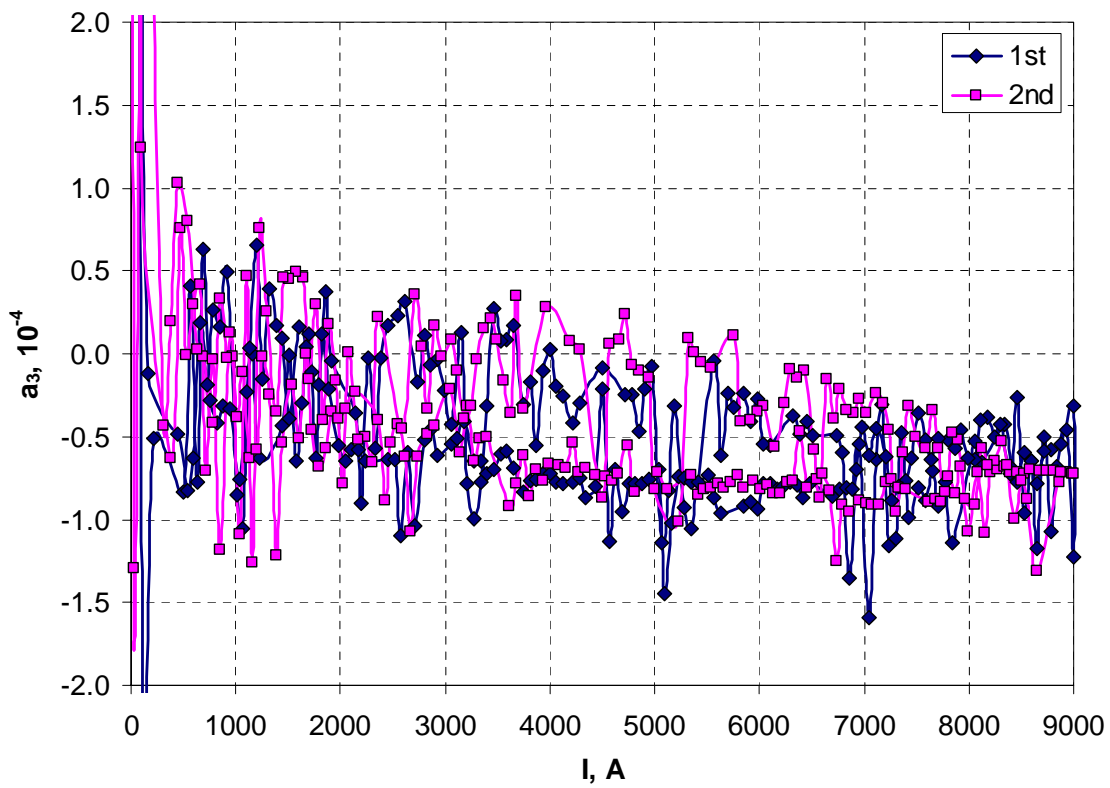


Figure 24. Skew sextupole as a function of current.

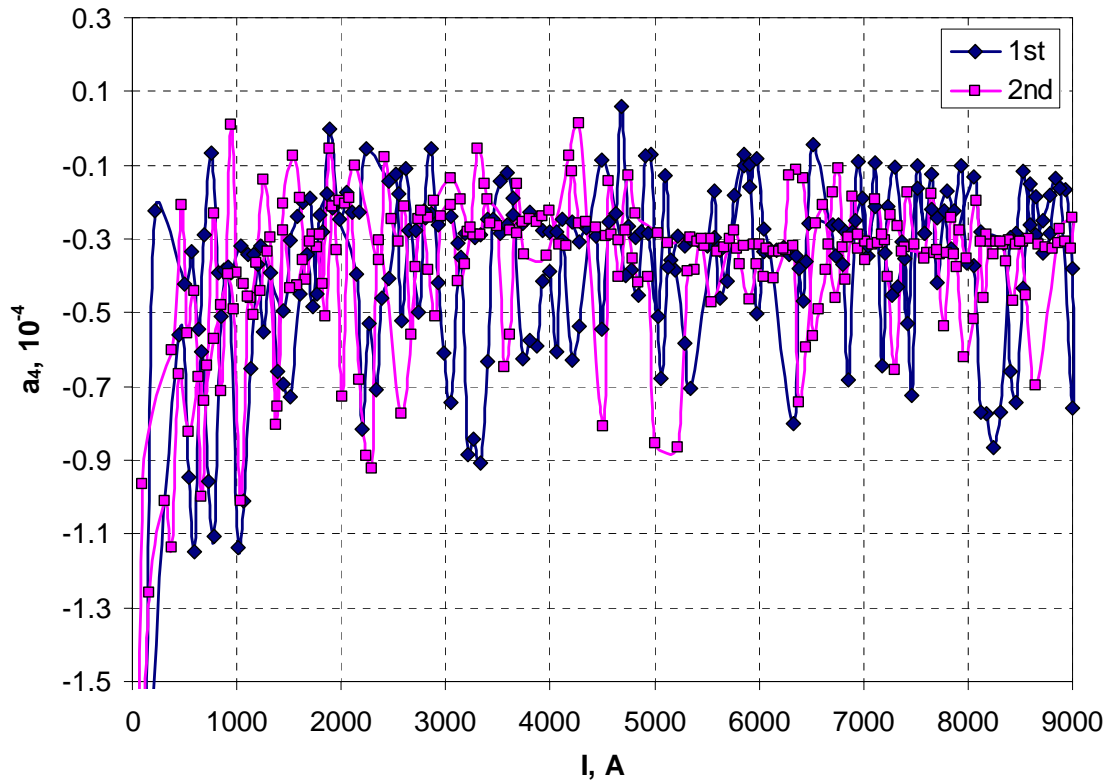


Figure 25. Skew octupole as a function of current.

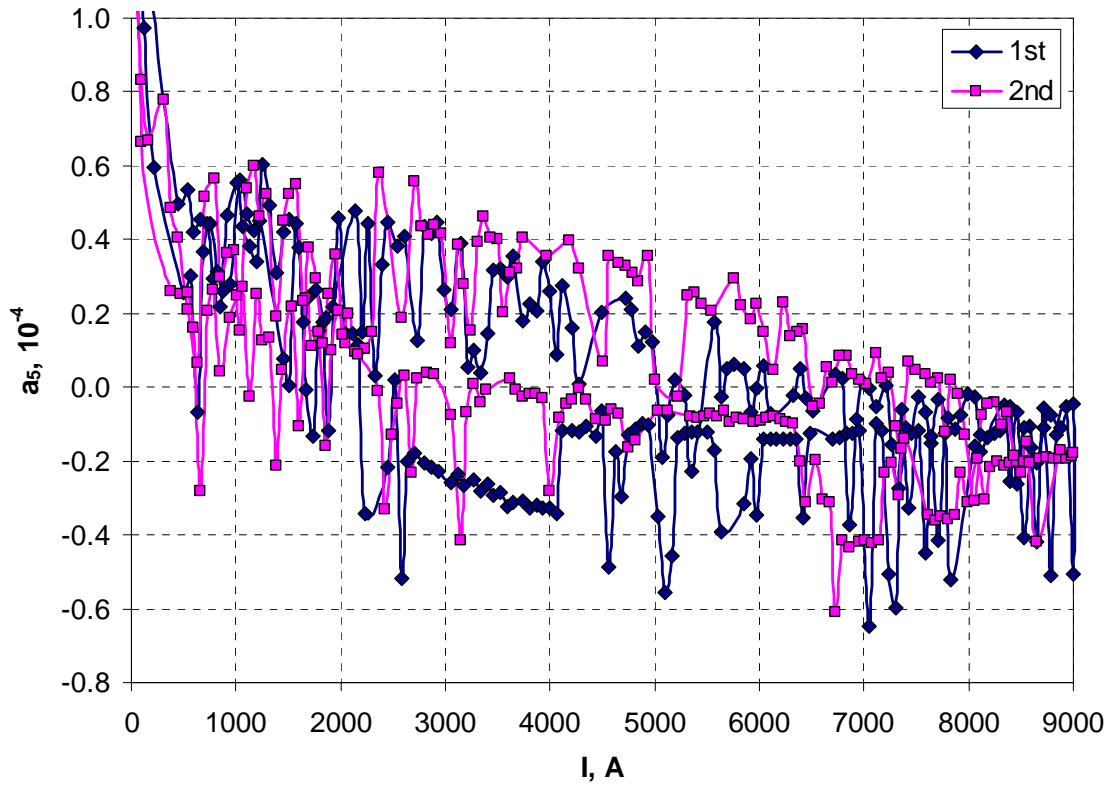


Figure 26. Skew decapole as a function of current.

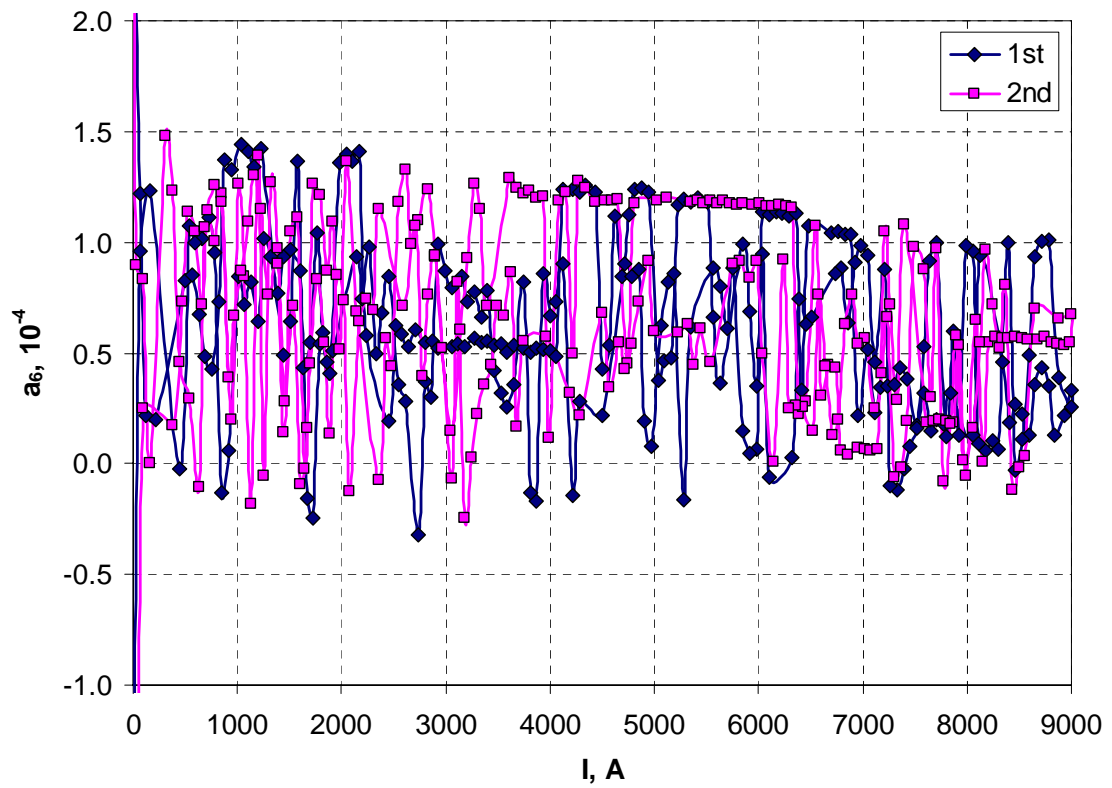


Figure 27. Skew dodecapole as a function of current.

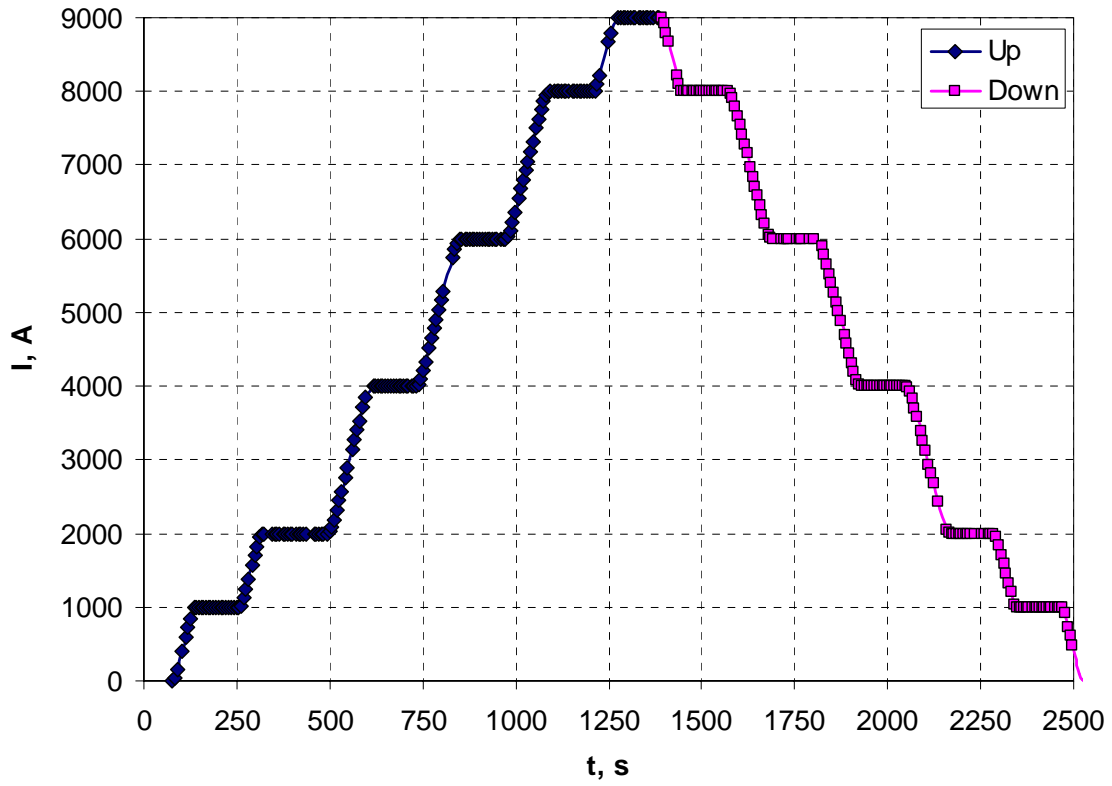


Figure 28. Magnet current as a function of time.

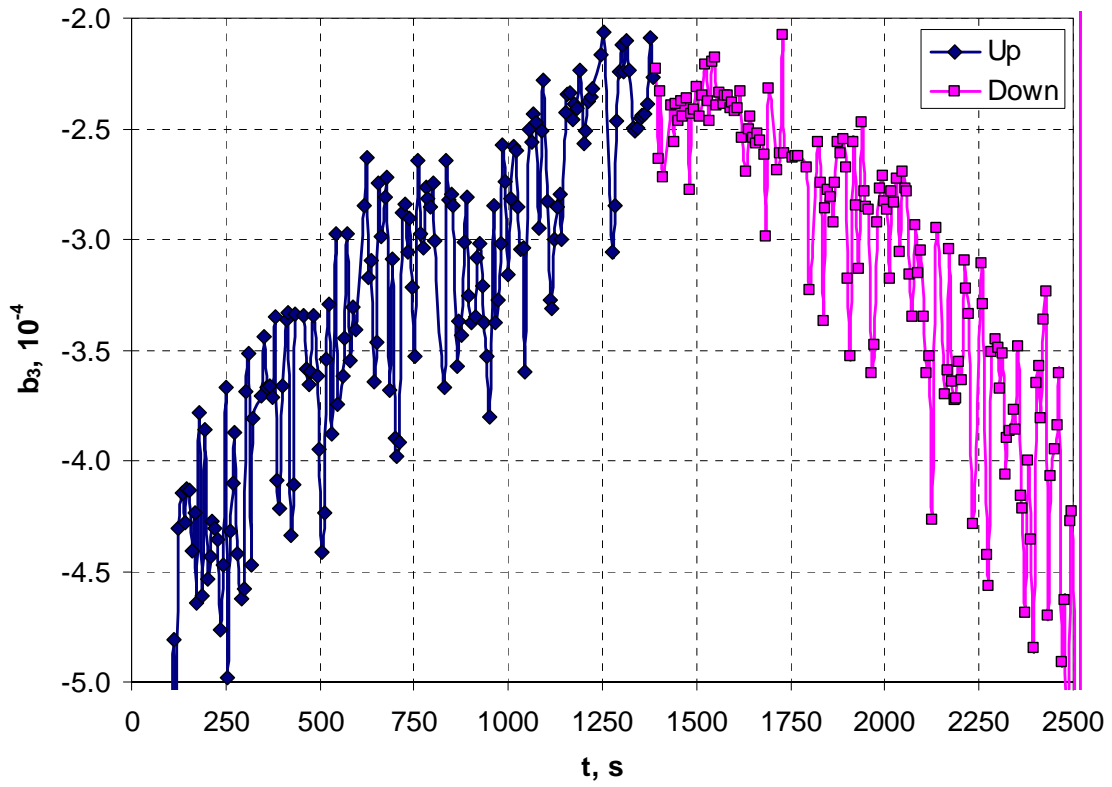


Figure 29. Normal sextupole as a function of time.

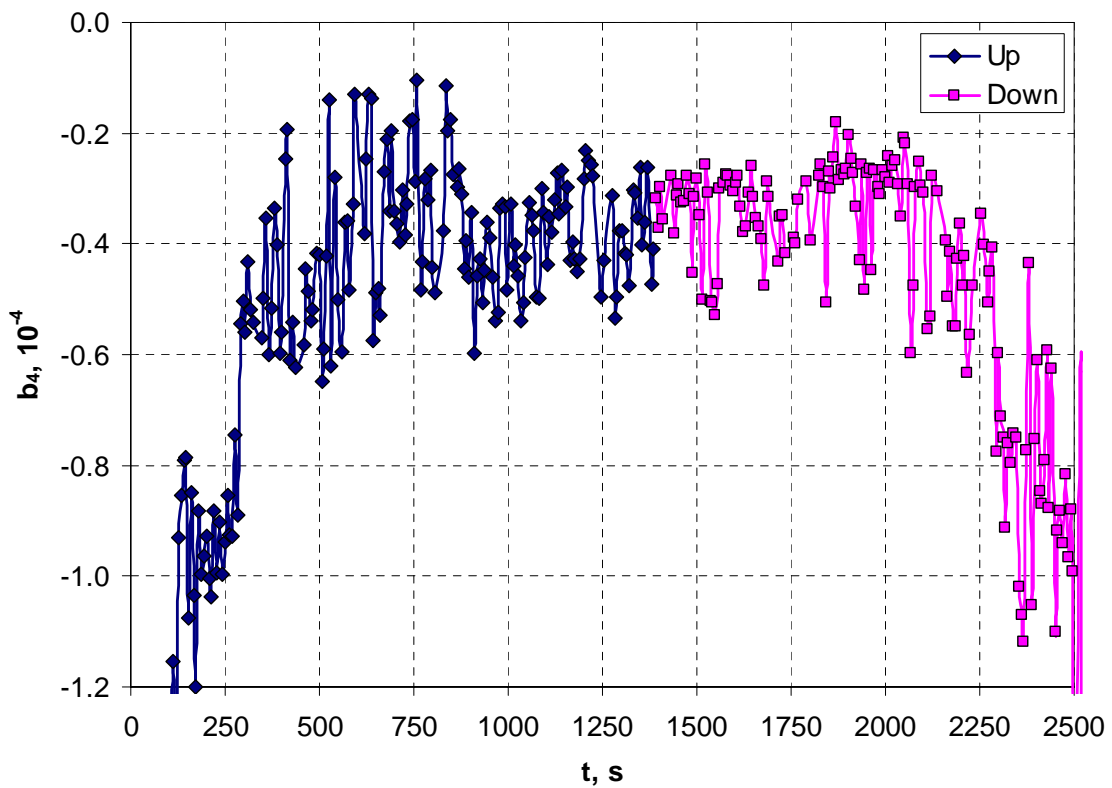


Figure 30. Normal octupole as a function of time.

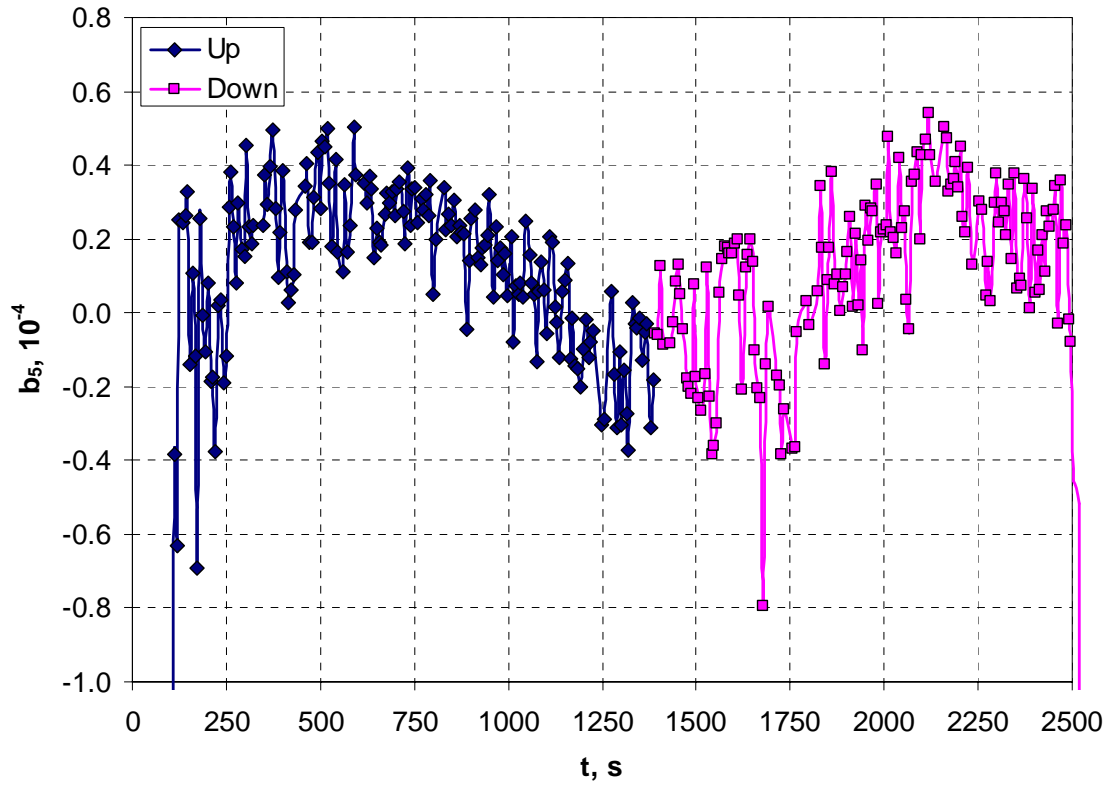


Figure 31. Normal decapole as a function of time.

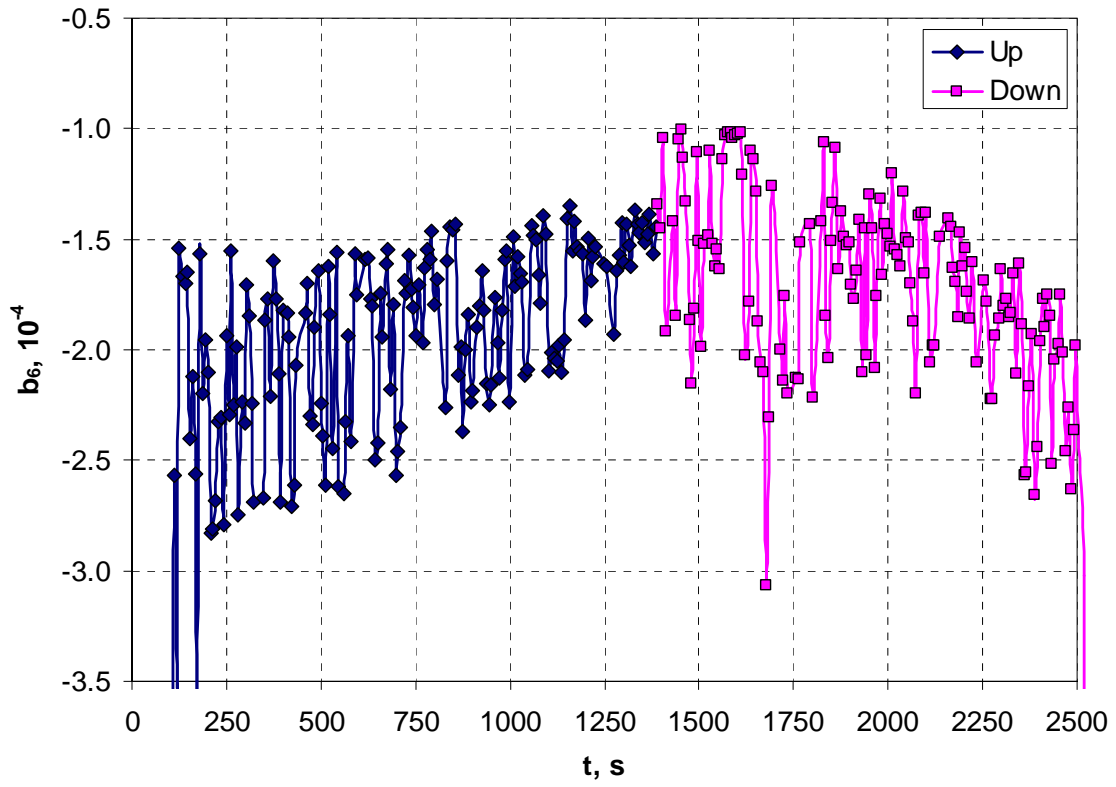


Figure 32. Normal dodecapole as a function of time.

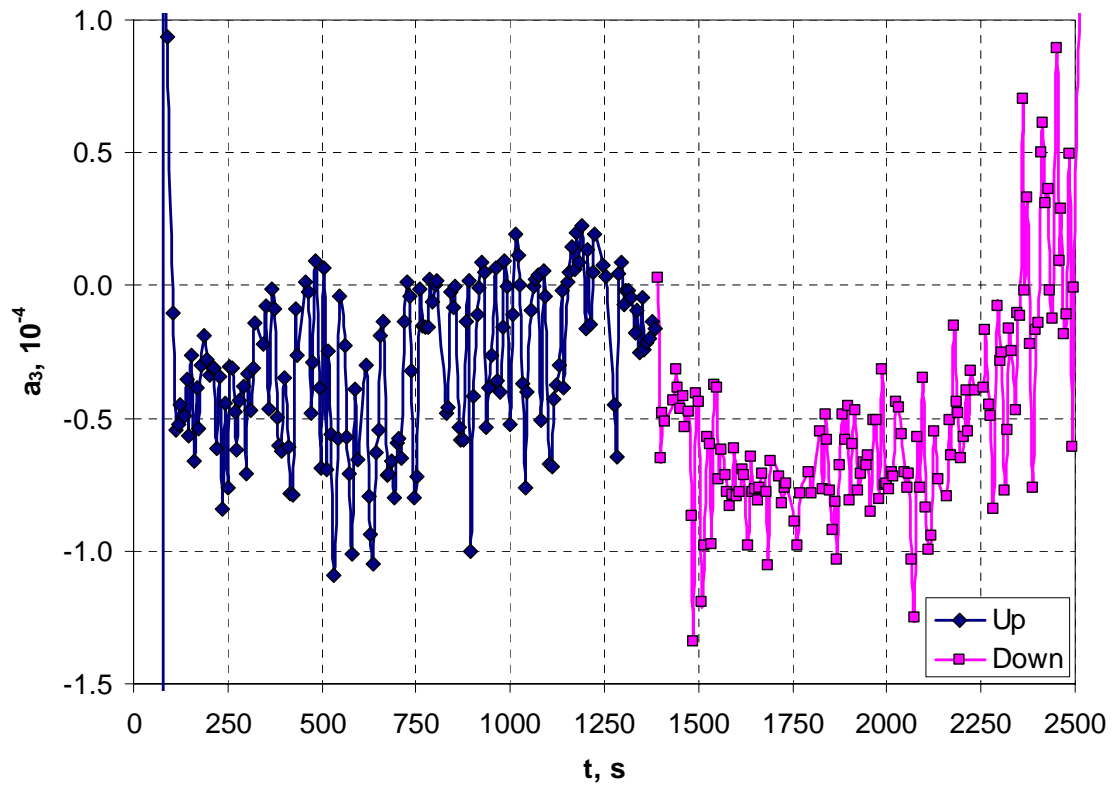


Figure 33. Skew sextupole as a function of time.

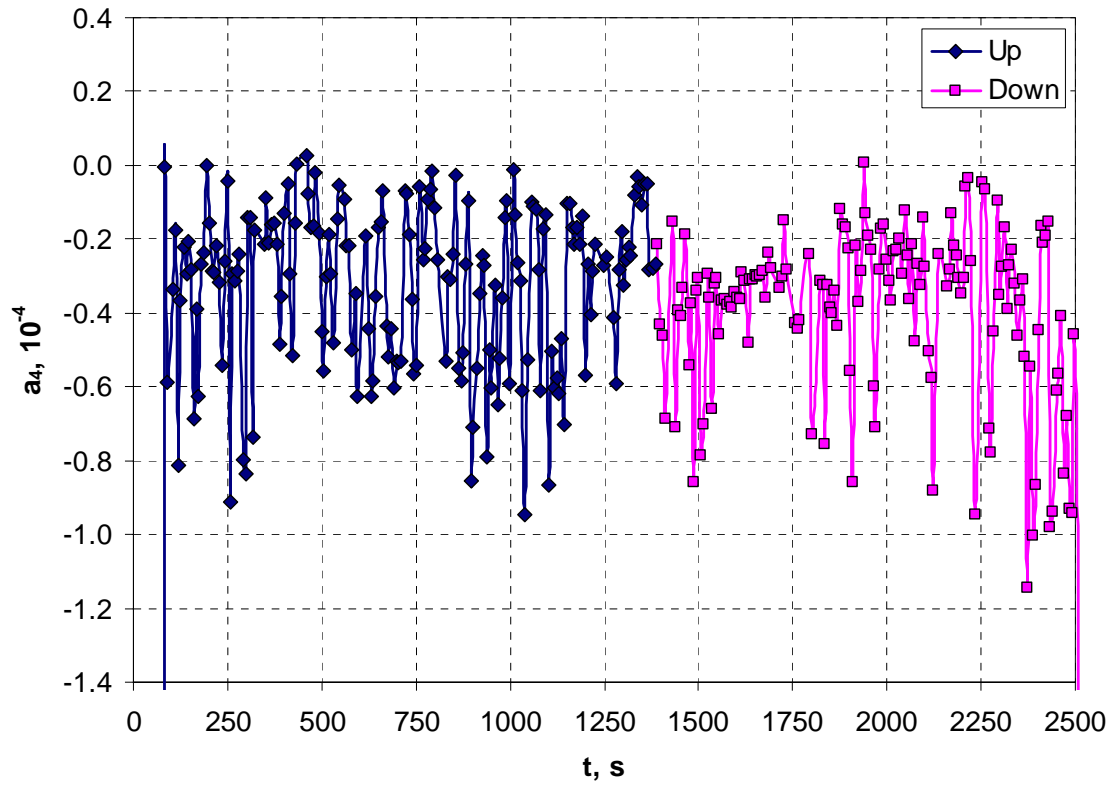


Figure 34. Skew octupole as a function of time.

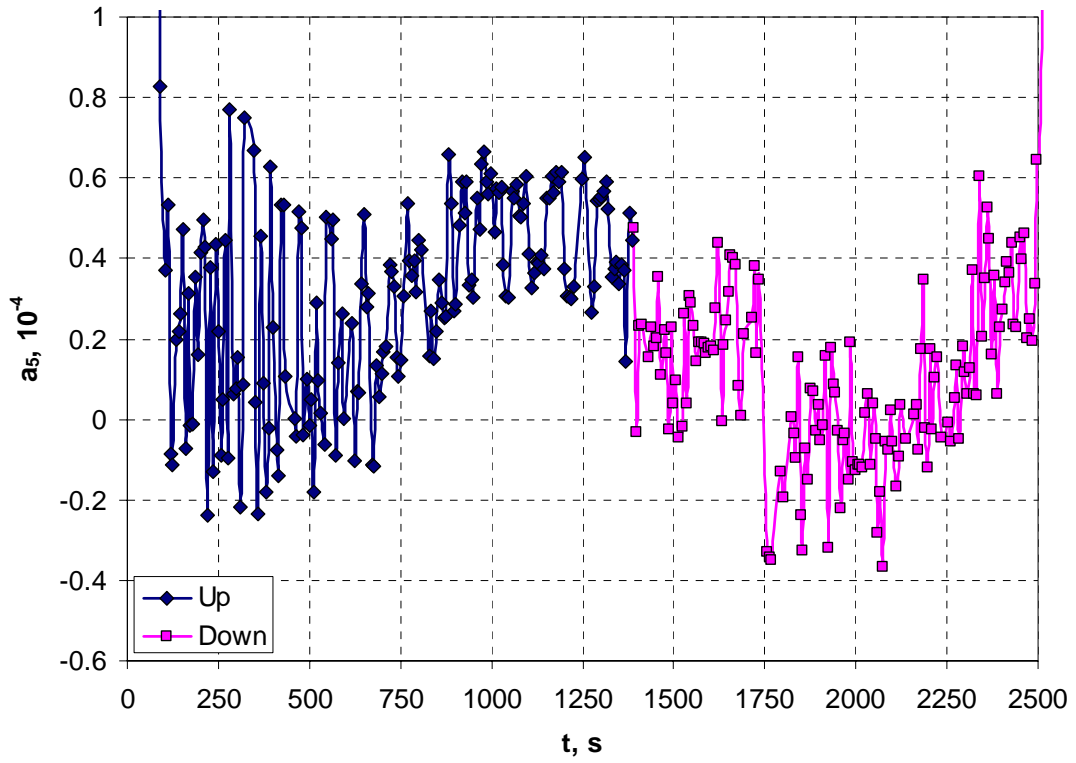


Figure 35. Skew decapole as a function of time.

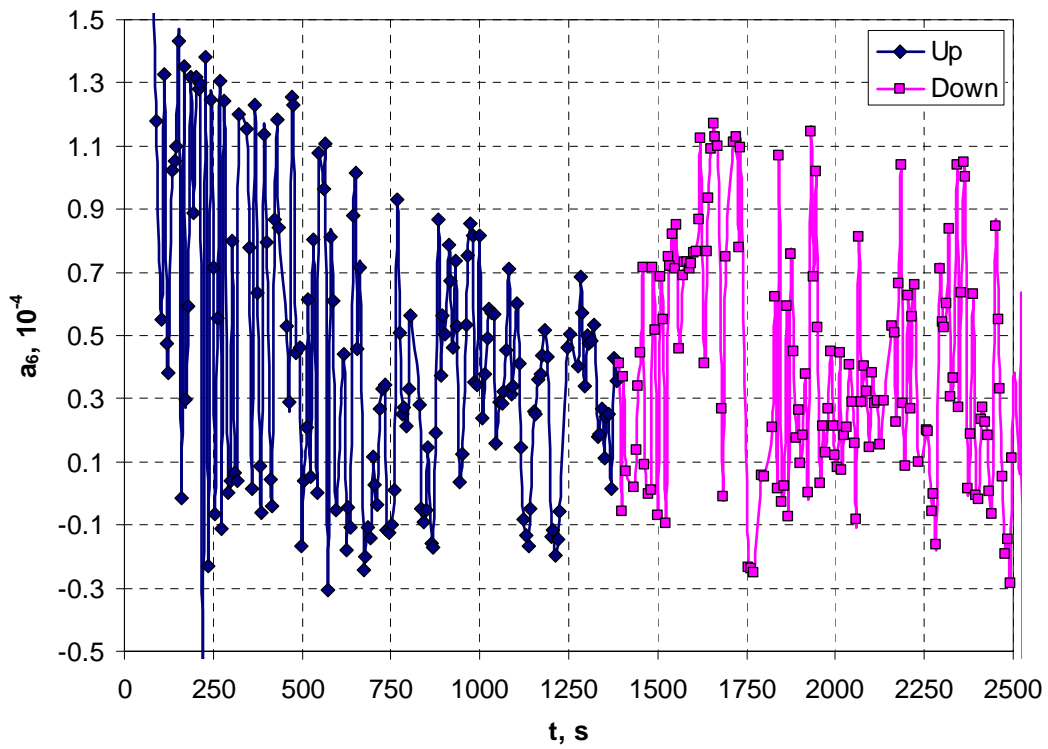


Figure 36. Skew dodecapole as a function of time

7. Strain gauges results

Instrumentation details

The subscale quadrupole SQ01 is instrumented with several strain gauges (see Table III) to measure the stress in the shell, in the aluminum rods, and in two of the four coils (SC15 and SC16).

TABLE III
STRAIN GAUGES

Gauge name	Gauge type	Gauge location	Measured strain
M01-15	Half-bridge	Shell, mid-plane, coils 01-15	ϵ_{θ}
M02-16	Half-bridge	Shell, mid-plane, coils 02-16	ϵ_{θ}
M15-02	Half-bridge	Shell, mid-plane, coils 15-02	ϵ_{θ}
M16-01	Half-bridge	Shell, mid-plane, coils 16-01	ϵ_{θ}
Z02-16	Half-bridge	Shell, mid-plane, coils 02-16	ϵ_z
Z15-01	Half-bridge	Shell, mid-plane, coils 15-01	ϵ_z
AR01	Full-bridge	Rod, coil 01	ϵ_z
AR02	Full-bridge	Rod, coil 02	ϵ_z
AR15	Full-bridge	Rod, coil 15	ϵ_z
AR16	Full-bridge	Rod, coil 16	ϵ_z
15HS	Full-bridge	Coil 15, heater side	ϵ_z - ϵ_y
15LS	Full-bridge	Coil 15, lead side	ϵ_z - ϵ_y
15LE	Full-bridge	Coil 15, lead end	ϵ_z - ϵ_y
15RE	Full-bridge	Coil 15, return end	ϵ_z - ϵ_y
16HS	Full-bridge	Coil 16, heater side	ϵ_z - ϵ_y
16LS	Full-bridge	Coil 16, lead side	ϵ_z - ϵ_y
16LE	Full-bridge	Coil 16, lead end	ϵ_z - ϵ_y
16RE	Full-bridge	Coil 16, return end	ϵ_z - ϵ_y

The aluminum shell is instrumented with six half-bridge gauges: four measure the azimuthal strain of the shell (ϵ_{θ}), while the other two measure the axial strain (ϵ_z). The gauges are positioned at the four mid-planes in the center of the magnet ($z = 0$), and they all have a temperature compensation gauge associated with them.

Four additional full-bridge strain gauges are attached to the aluminum rods to measure the axial tension (ϵ_z).

Each of the two RRP coils is instrumented with four full-bridge strain gauges placed directly over the turns and impregnated with them (Fig. 37). Attaching strain gauges to coils and securing their position was done with a coil trace overlay. The trace, a ProE (CAD) drawing, included four full-bridge strain gauges, a spot-heater, and several voltage-taps. Drawn on vellum paper, the trace was subjected to a photo etch process that resulted in a 25 μm thick stainless image over a 50 μm thick Kapton sheet. Micro-

measurements full bridge strain gauges (350Ω, SK-13-120NB-350) were used to replace cutout marked squares on the Kapton sheet. The gauges were aligned and soldered to the Kapton trace using short copper wires. The gauges are located in the two coil straight sections (heater side HS and lead side LS) and in the two coil ends (lead end LE and return end RE), and they measure the difference between axial and vertical strain ($\epsilon_z - \epsilon_y$). On the straight section the axial and vertical directions are respectively along and across the turns. On the other hand, in the end region the axial and vertical directions are respectively across and along the turns.

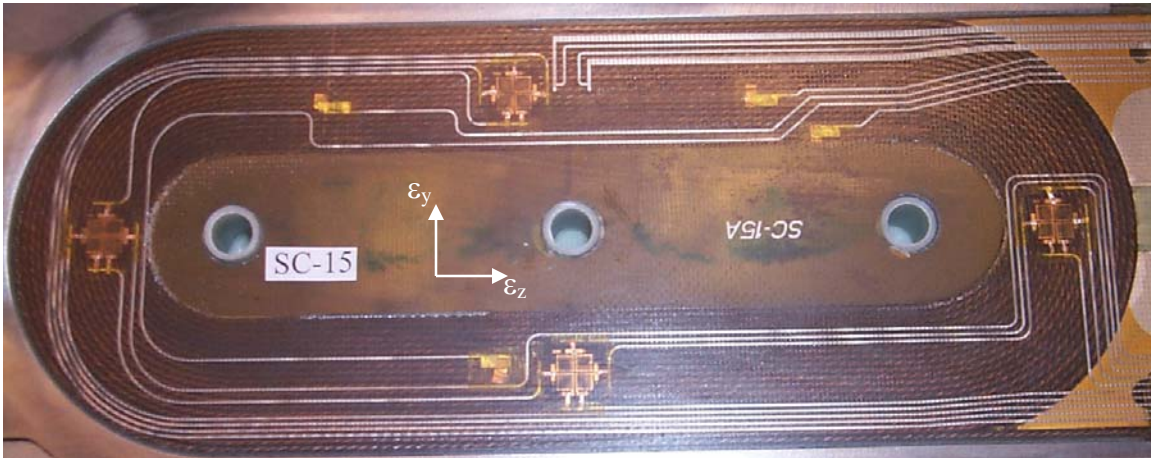


Fig. 37. Strain gauge location on coil SC15 (with strain orientation).

Measurements schedule

The strain gauge readings presented in this report have been performed after the assembly at LBNL (room temperature values), and after the cool-down and during ramp-up at FNAL (4.5 K and magnet excitation values). In particular, during the ramping, the strain in the magnet components have been recorded every 6 second: we report in this paper the strain variation as a function of Lorentz force for quench #2, #3, #4, #5, #6, #7, #8, #9, and #10, performed on 01/19/05.

Results

Aluminum shell

The azimuthal stress variations in the shell during cool-down are depicted in Fig. 38 and Fig. 39: with the exception of gauge M01-15, which provides a 25 % lower strain at 4.5 K (the same behavior was observed in the cool-down during the first magnet test at LBNL), three azimuthal gauges measure an average stress (tension) variation during cool-down from 40 MPa to 120 MPa. The stretching of the shell from 293 K to 4.5 K along the azimuthal direction determines an axial contraction (Fig. 39), due to Poisson effect.

In Fig. 40-45 the stress/strain variation versus time and as a function of the fraction of Lorentz force with respect to the 4.3 K short sample value ($(I/I_{ss})^2$), both for the azimuthal and the axial direction, are plotted. During excitation, the electromagnetic forces in the straight section push the conductors towards the mid-plane, unloading the pole. This

produces an increase of azimuthal tension in the shell (within 1 MPa, Fig. 44), with a corresponding slight contraction along the axial direction (about 20 micro-strains, Fig. 45).

After a ramp-up, when the Lorentz force vanishes, it has often been observed that the strain in the mechanical structure is different than the original unloaded condition: in particular, a positive residual strain is measured for the axial rods, and a negative one is measured for the shell. This phenomenon is usually referred as ratcheting. Fig 46 and Fig. 47 compare the stress/strain in the shell during ramp #2 and ramp #10: a small reduction of tension is observed in the shell, while the axial strain appears to remain unchanged.

Aluminum rods

The stress measurements indicate a change in the average tension of the rods during cool-down from 80 MPa to 150 MPa (Fig. 48), with an increase of about 4 MPa during excitation (Fig. 49-51). No significant residual stress is observed from quench #2 to quench #10 (Fig. 52).

Coil 15 and coil 16: straight section

The increase of coil pre-stress during cool-down results in a compression of the conductors in the straight section (negative ϵ_y), with an elongation along the axial direction (positive ϵ_z). The combination of these two effects determines an increase of the bidirectional strain (ϵ_z - ϵ_y) from an average of 650 micro-strains to an average of 4000 micro-strains (Fig. 53).

During excitation, the bidirectional strain further increases of about 200 micro-strains (Fig. 54-56): the variation may be explained by the fact that the Lorentz forces in the end region are directed outwards, thus increasing the axial strain in the straight section (positive ϵ_z). The effect is well reproducible in three strain gauges (15HS, 16HS, and 16LS), with 50 micro-strains of residual strain observed from quench #2 to quench #10 (Fig. 57). On the other hand, gauge 15LS shows a significant strain change after quench #5.

Coil 15 and coil 16: end region

The strain measurements in the coil end regions performed during cool-down (Fig. 58) present a general decrease of the bidirectional strain of the order of 1000 micro-strains, with significant offsets among the four strain gauges. The trend can be explained by the fact that the force provided by the rods increases significantly during cool-down. As a consequence, the coil end regions, at 4.5 K, are more compressed along the axial direction (negative ϵ_z), and deformed along the y direction (negative ϵ_y).

The behavior is enhanced during excitation (Fig. 59-61), when the bidirectional strain decreases of about 1500 micro-strains, with a residual strain from quench #2 to quench #10 of about 100 micro-strains (Fig. 62). Also in the end region, an abrupt strain change is measured in coil 15 at quench #5.

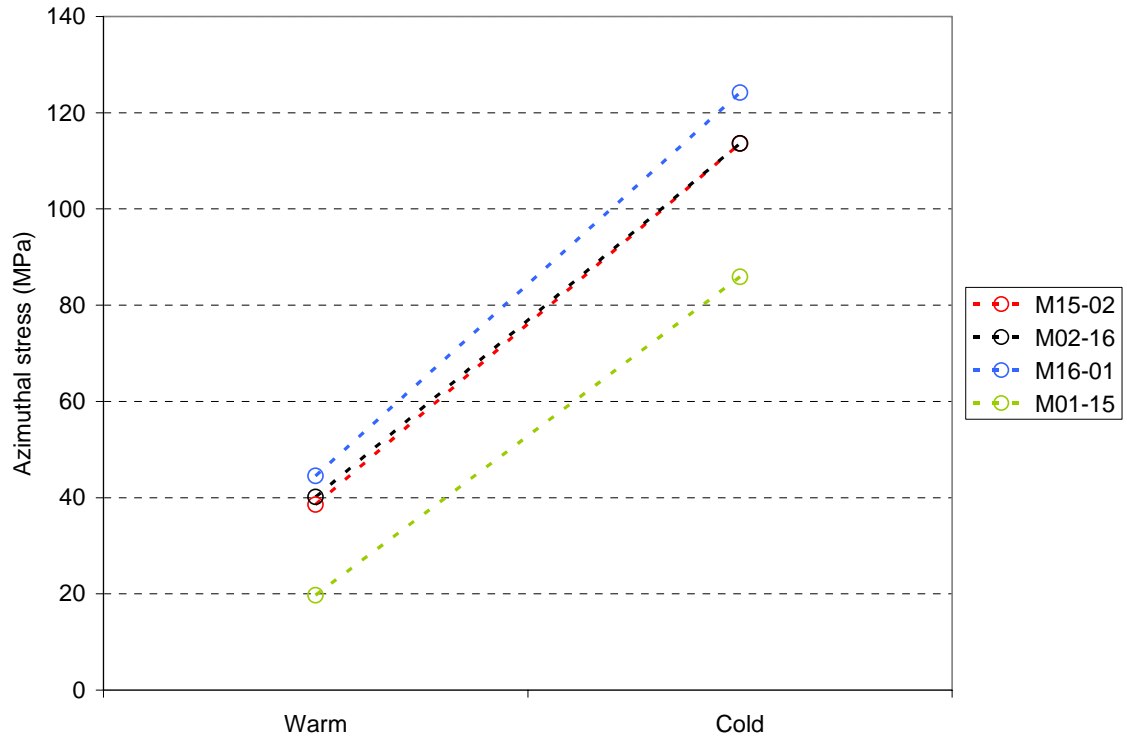


Fig. 38. Azimuthal stress (MPa) in the shell during cool-down.

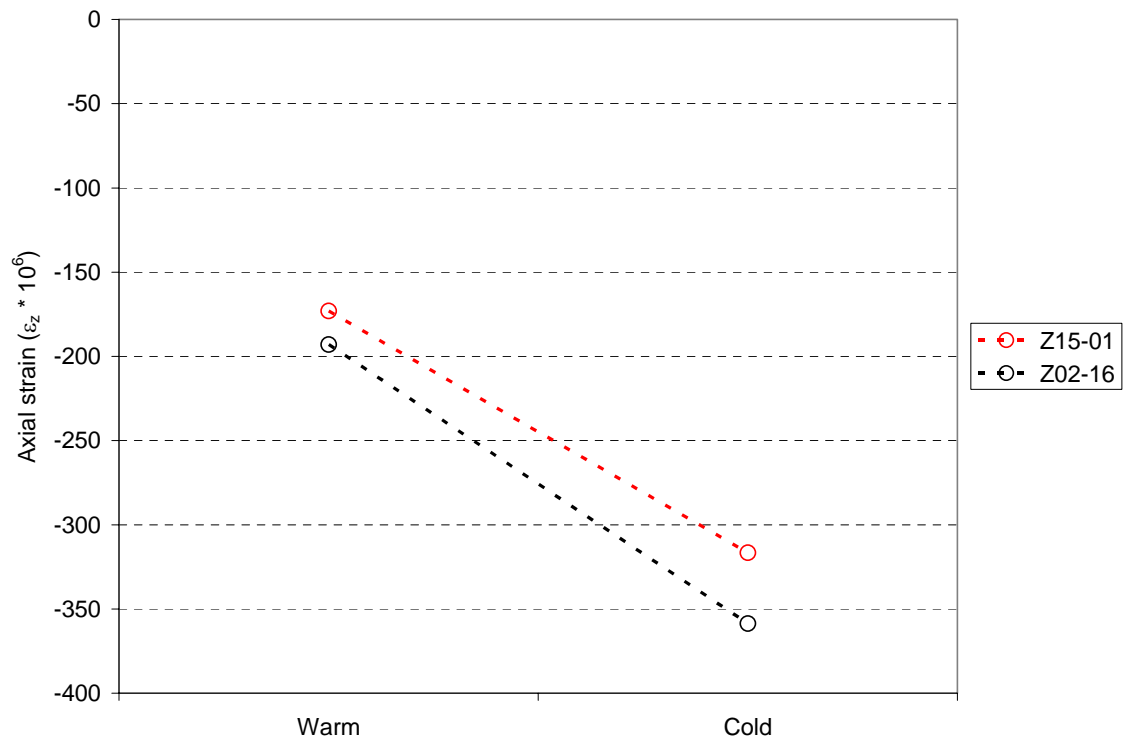


Fig. 39. Axial strain ($\cdot 10^6$) in the shell during cool-down.

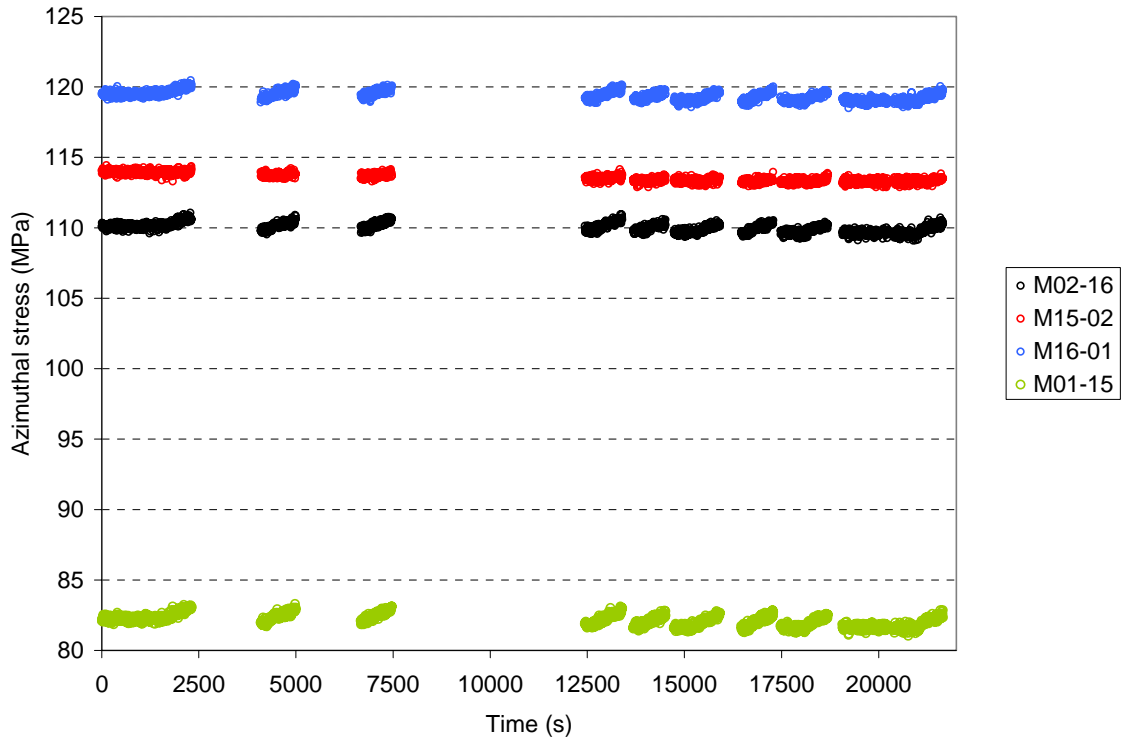


Fig. 40. Azimuthal stress (MPa) in the shell during magnet excitation as a function of time (s).

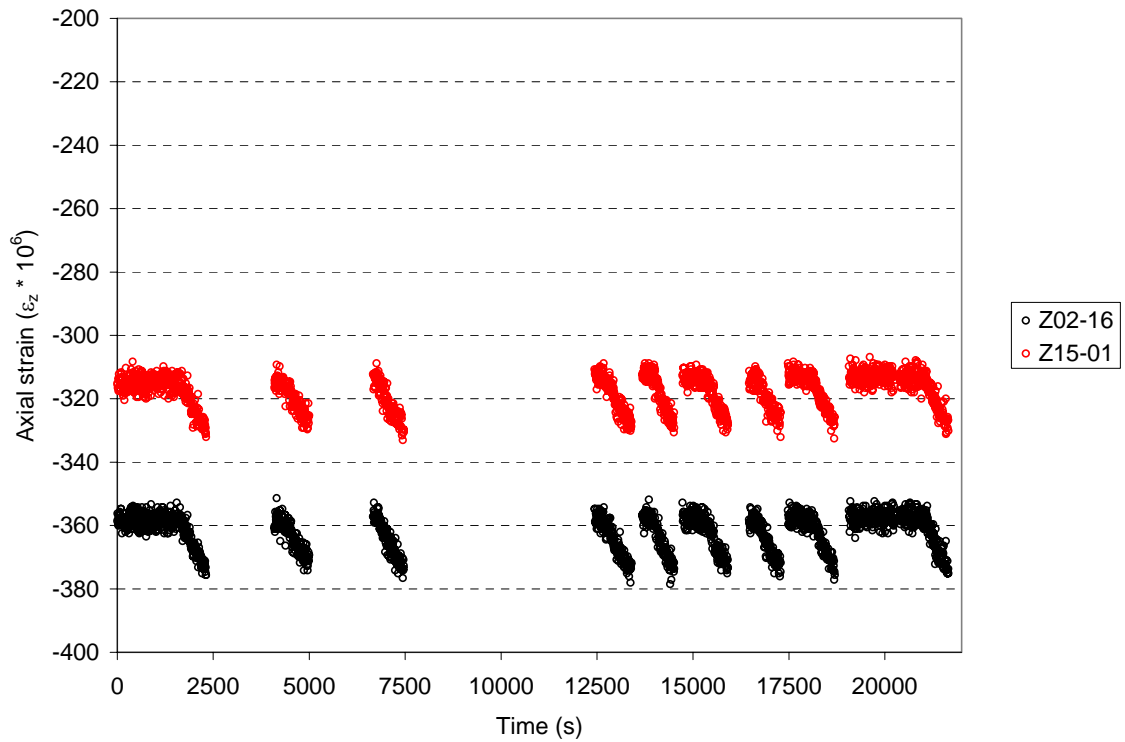


Fig. 41. Axial strain ($\cdot 10^6$) in the shell during magnet excitation as a function of time (s).

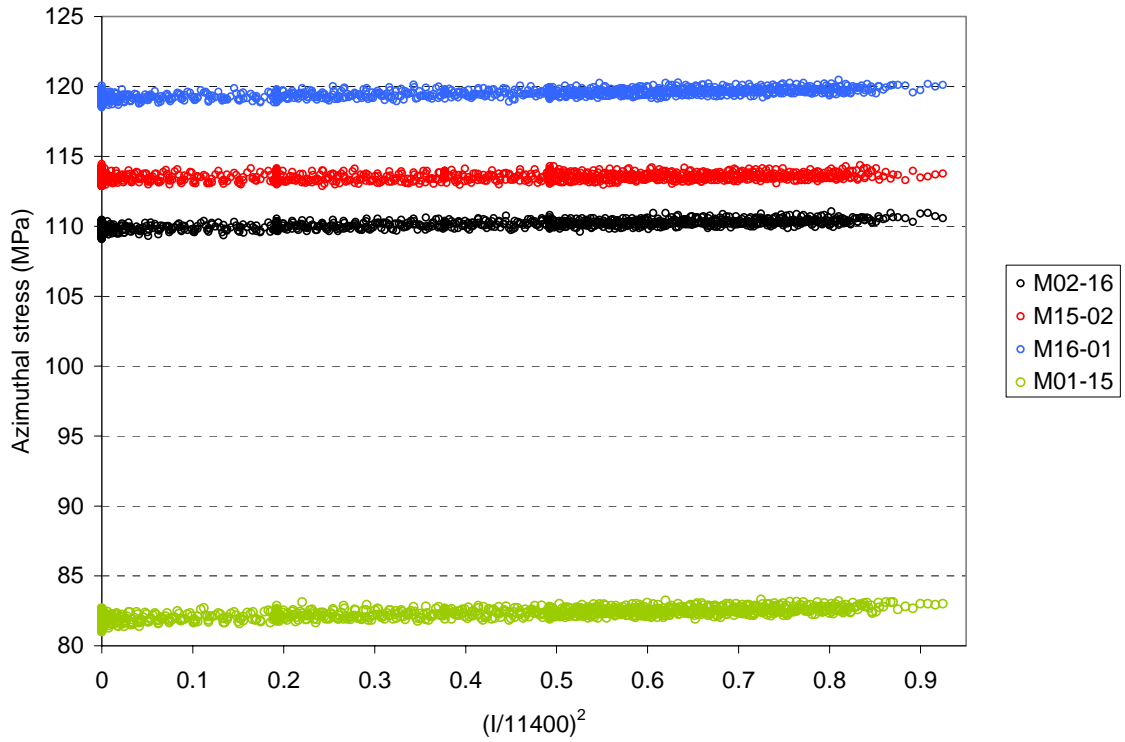


Fig. 42. Azimuthal stress (MPa) in the shell during magnet excitation as a function of the fraction of Lorentz force with respect to short sample.

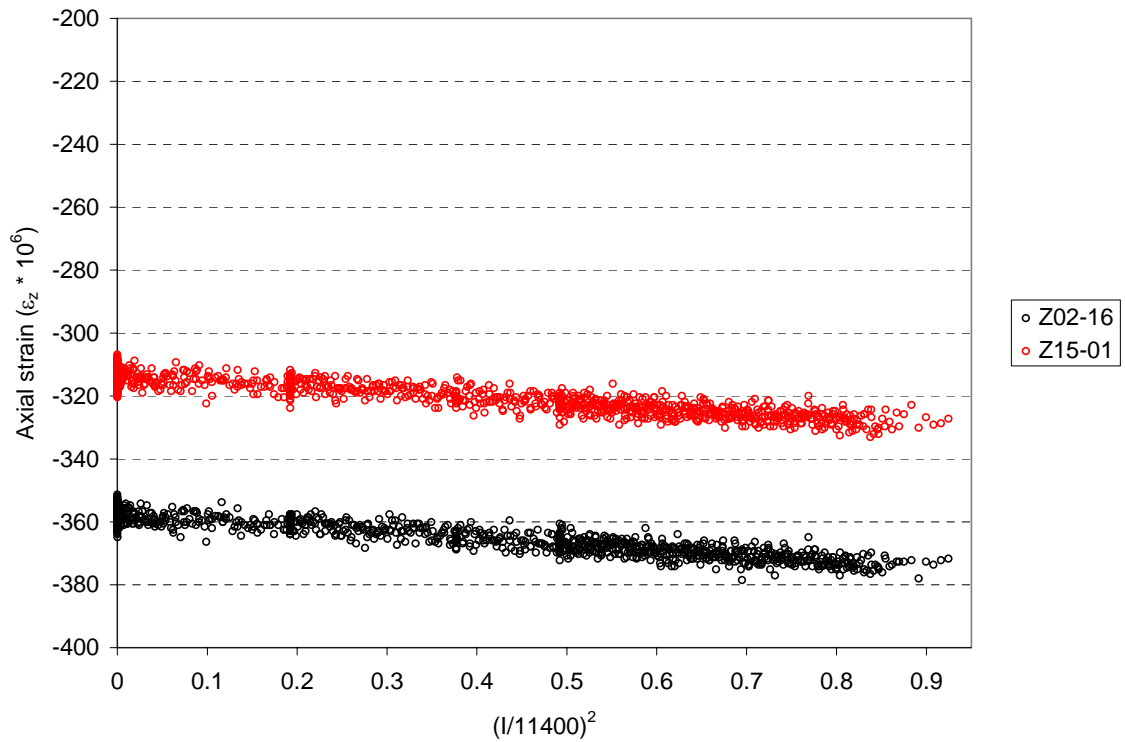


Fig. 43. Axial strain ($\cdot 10^6$) in the shell during magnet excitation as a function of the fraction of Lorentz force with respect to short sample.

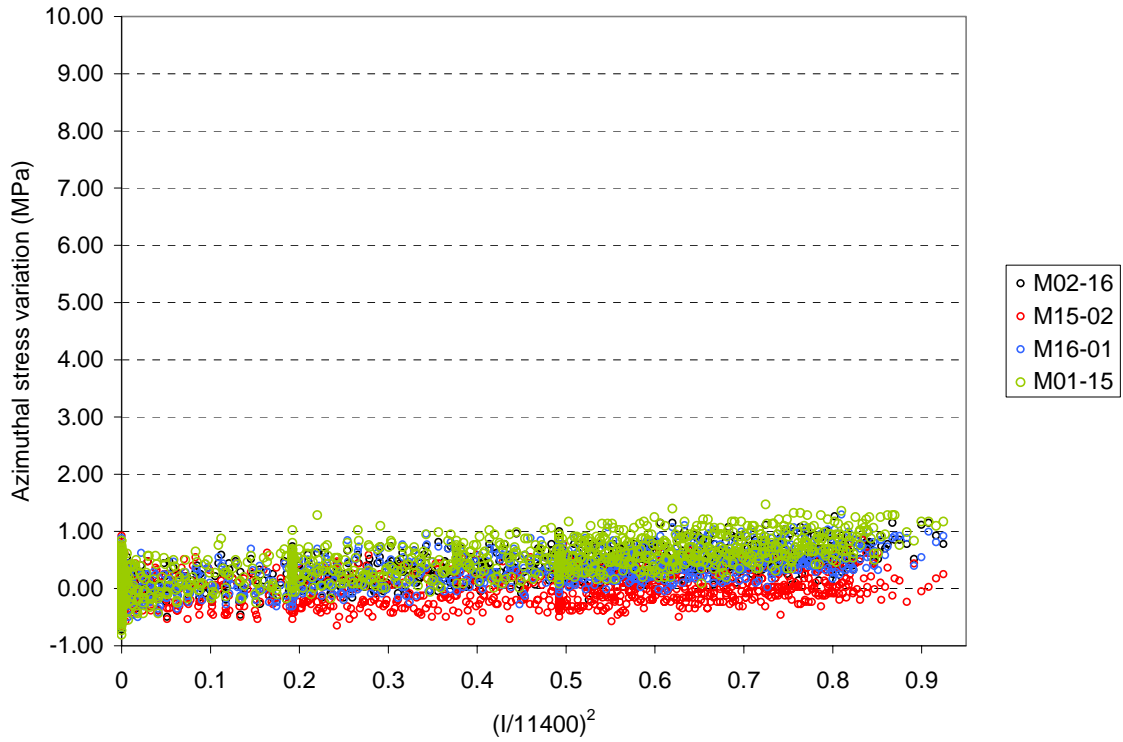


Fig. 44. Variation of azimuthal stress (MPa) in the shell during magnet excitation as a function of the fraction of Lorentz force with respect to short sample.

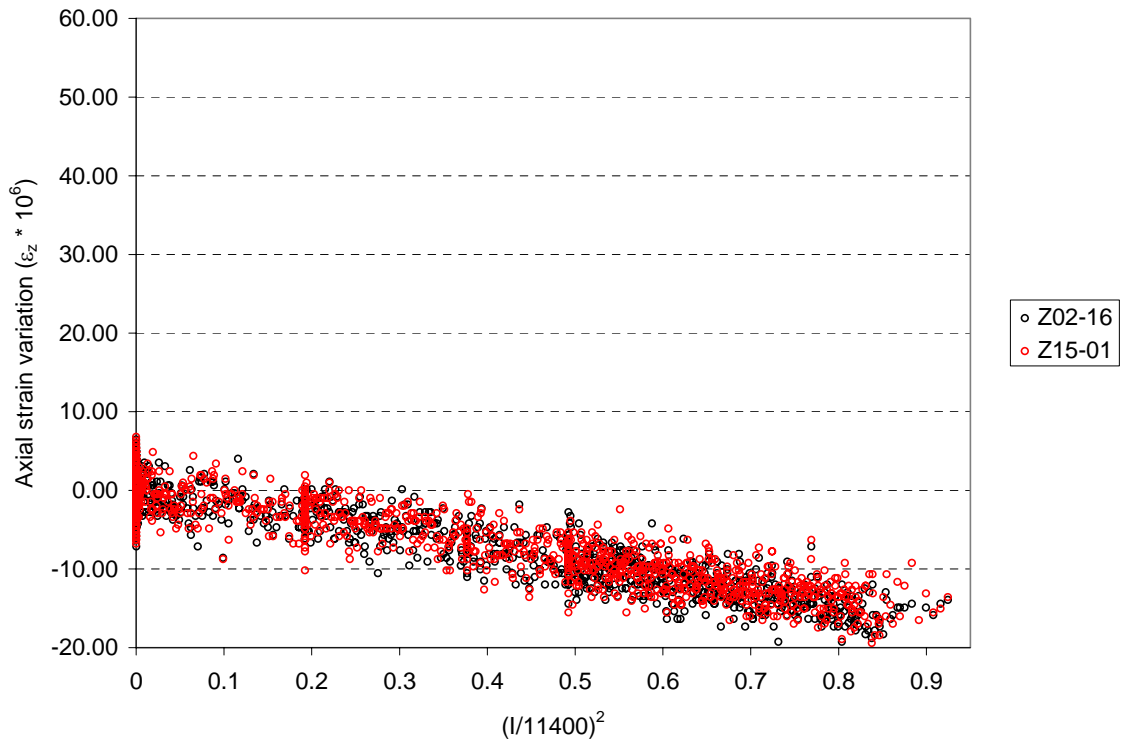


Fig. 45. Variation of axial strain ($\cdot 10^6$) in the shell during magnet excitation as a function of the fraction of Lorentz force with respect to short sample.

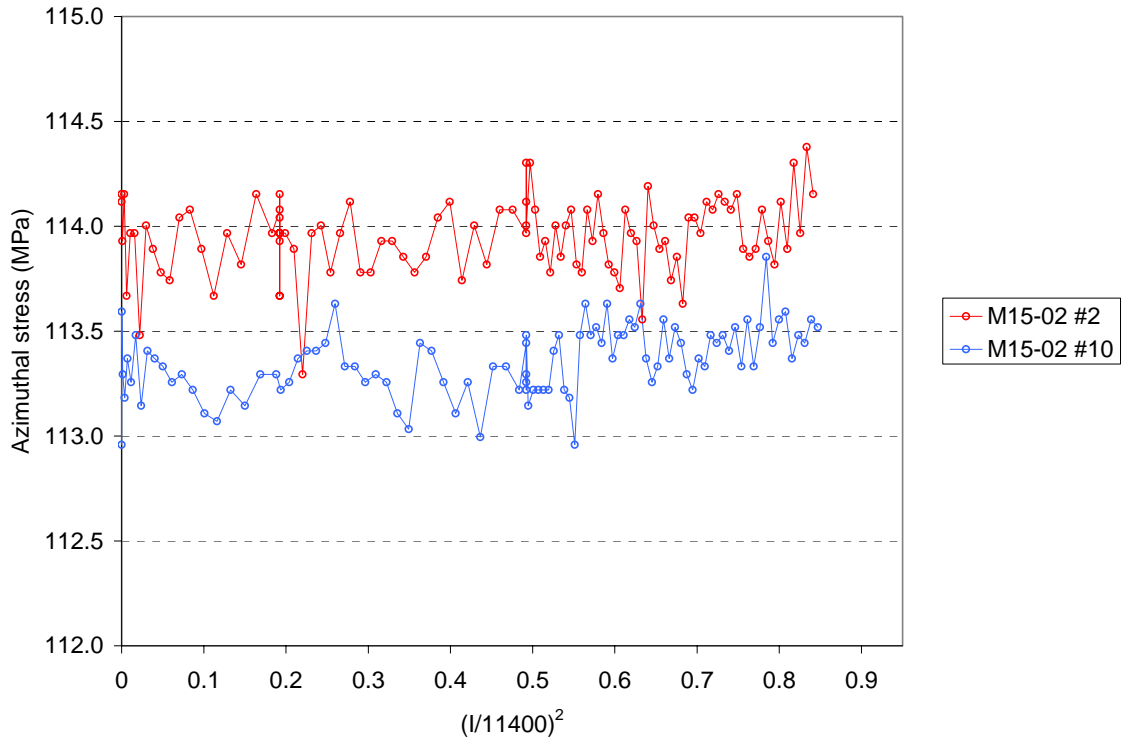


Fig. 46. Azimuthal stress (MPa) in the shell during magnet excitation as a function of the fraction of Lorentz force with respect to short sample: quench #2 and quench #10.

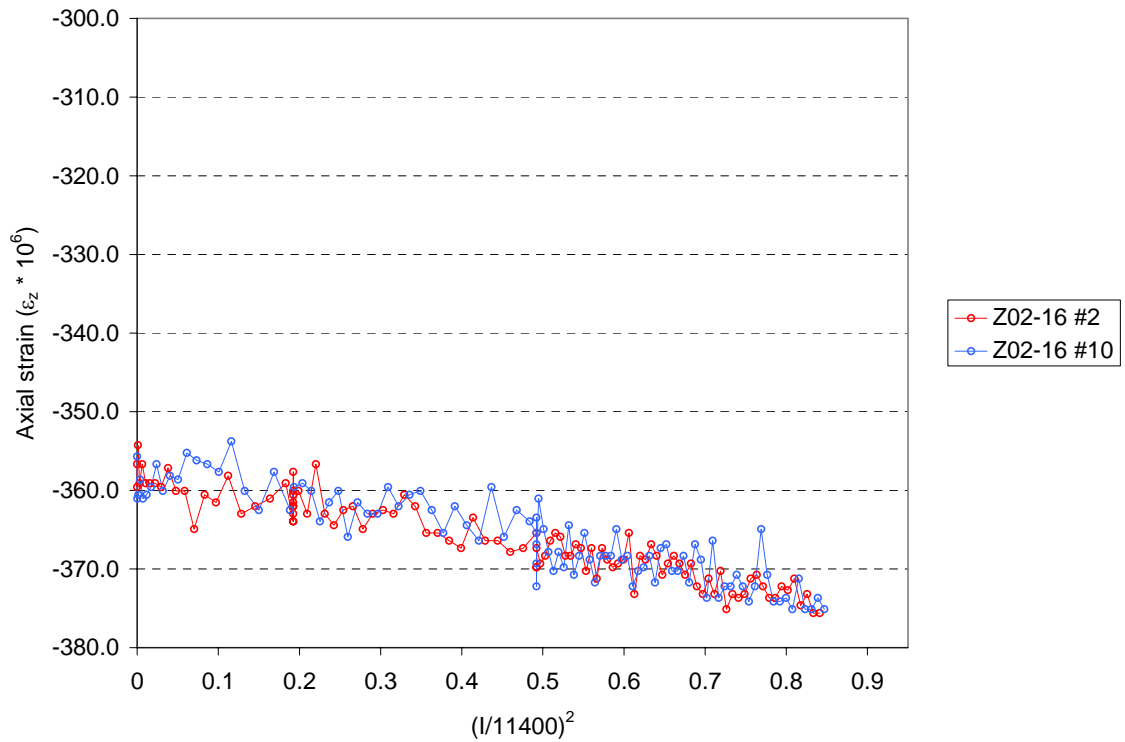


Fig. 47. Axial strain ($\cdot 10^6$) in the shell during magnet excitation as a function of the fraction of Lorentz force with respect to short sample: quench #2 and quench #10.

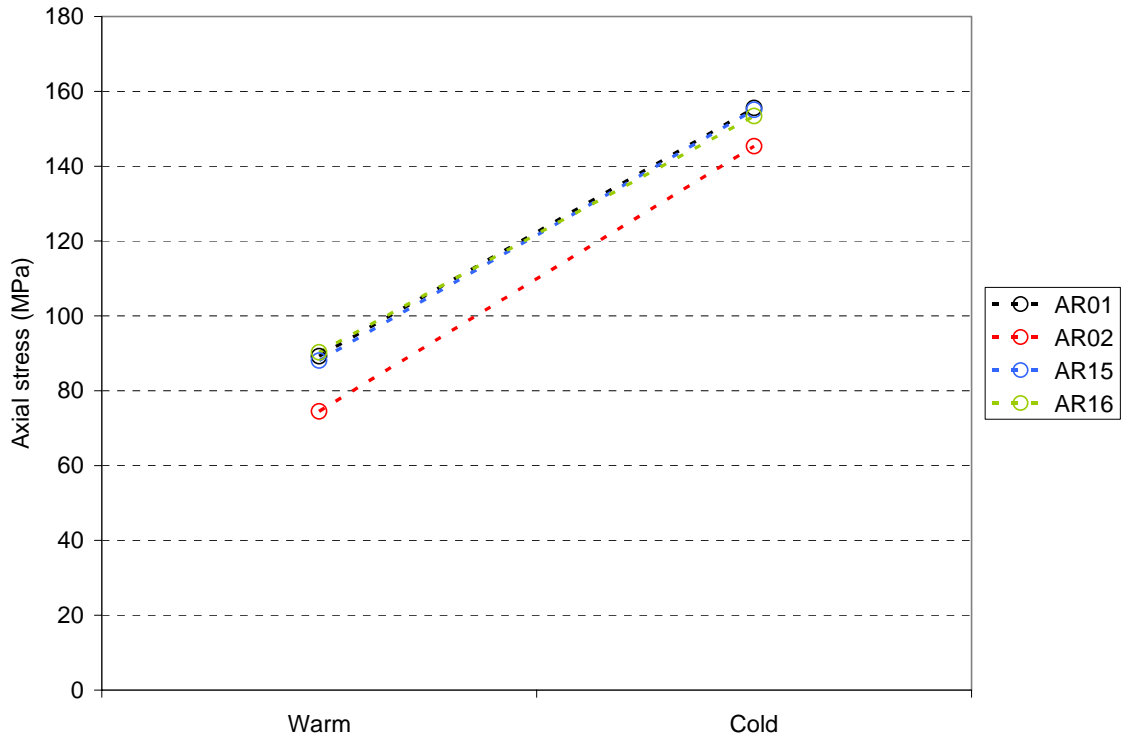


Fig. 48. Axial stress (MPa) in the rods during cool-down.

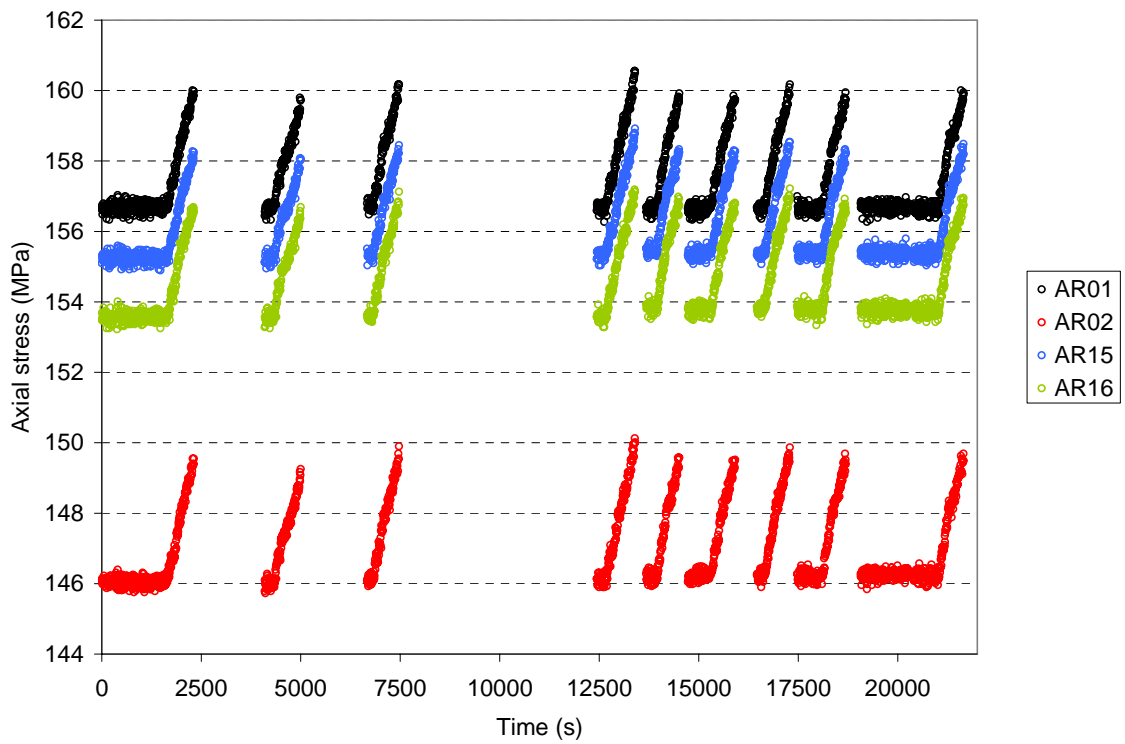


Fig. 49. Axial stress (MPa) in the rods during magnet excitation as a function of time (s).

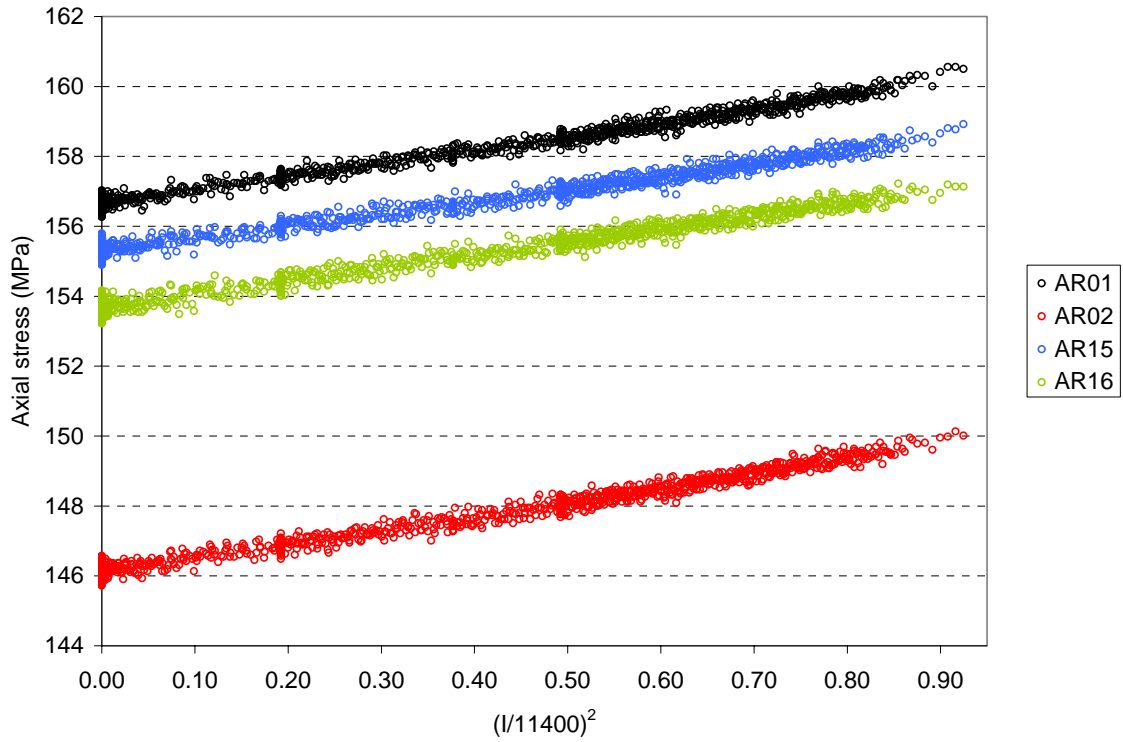


Fig. 50. Axial stress (MPa) in the rods during magnet excitation as a function of the fraction of Lorentz force with respect to short sample.

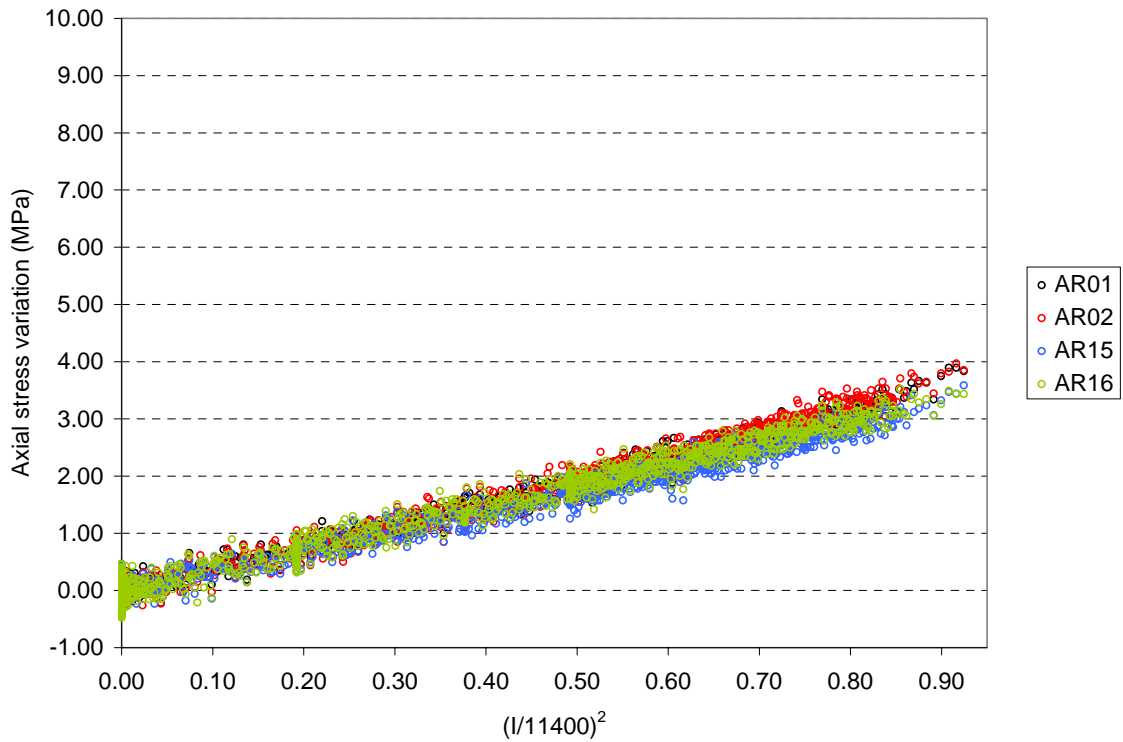


Fig. 51. Variation of axial stress (MPa) in the rods during magnet excitation as a function of the fraction of Lorentz force with respect to short sample.

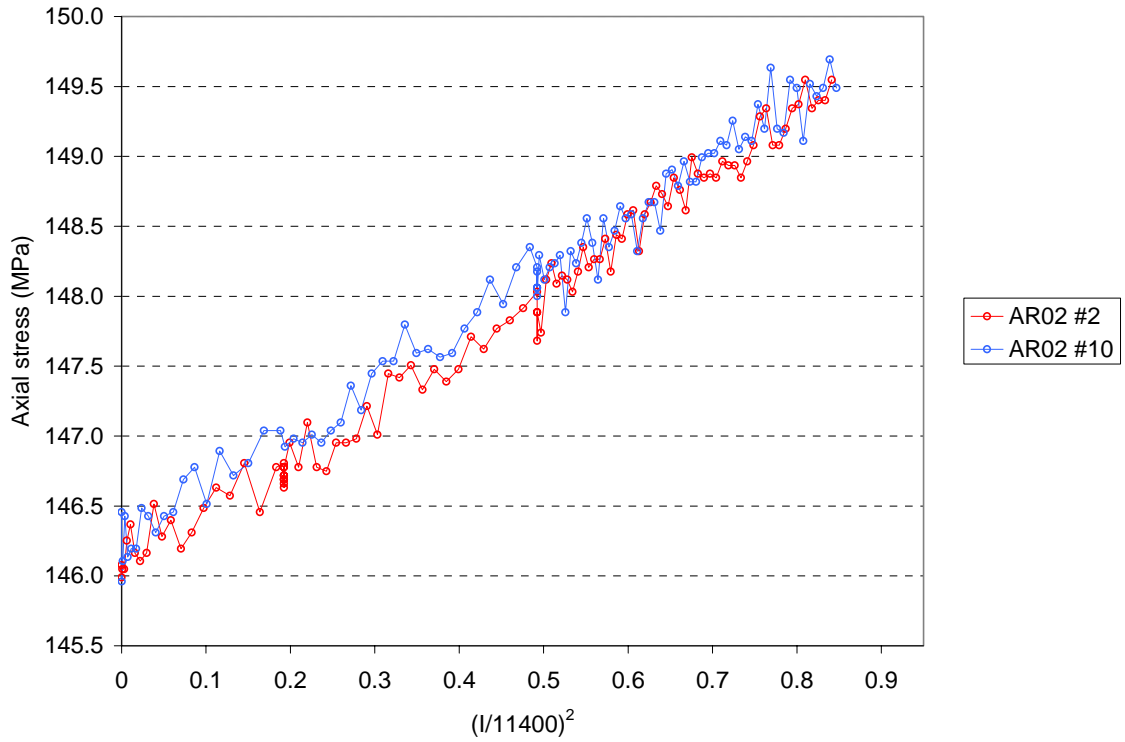


Fig. 52. Axial stress (MPa) in the rods during magnet excitation as a function of the fraction of Lorentz force with respect to short sample: quench #2 and quench #10.

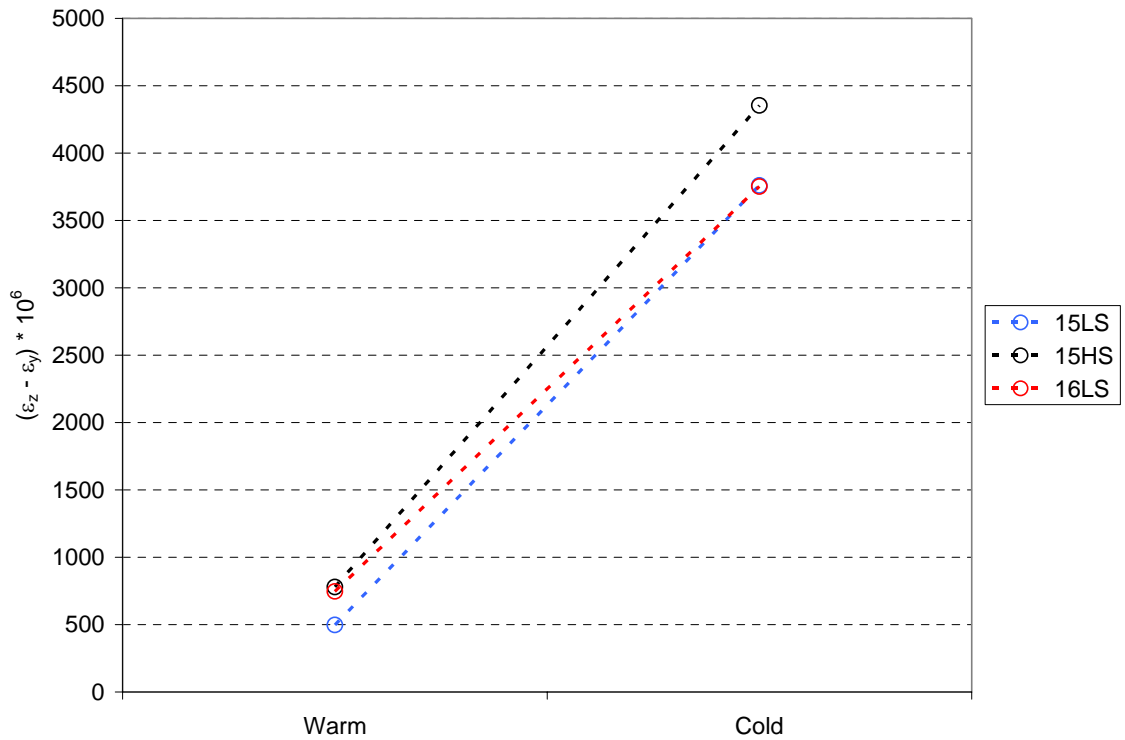


Fig. 53. Strain difference ($\cdot 10^6$) in the coil straight sections during cool-down.

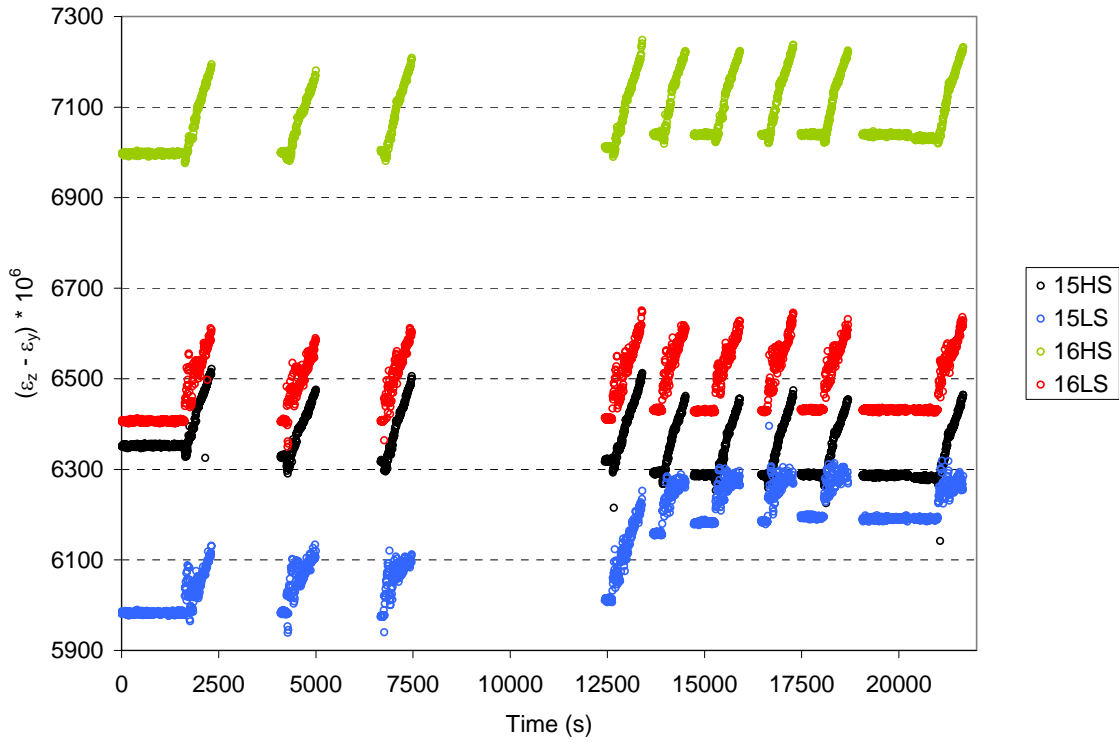


Fig. 54. Strain difference ($\cdot 10^6$) in the coil straight sections during magnet excitation as a function of time (s).

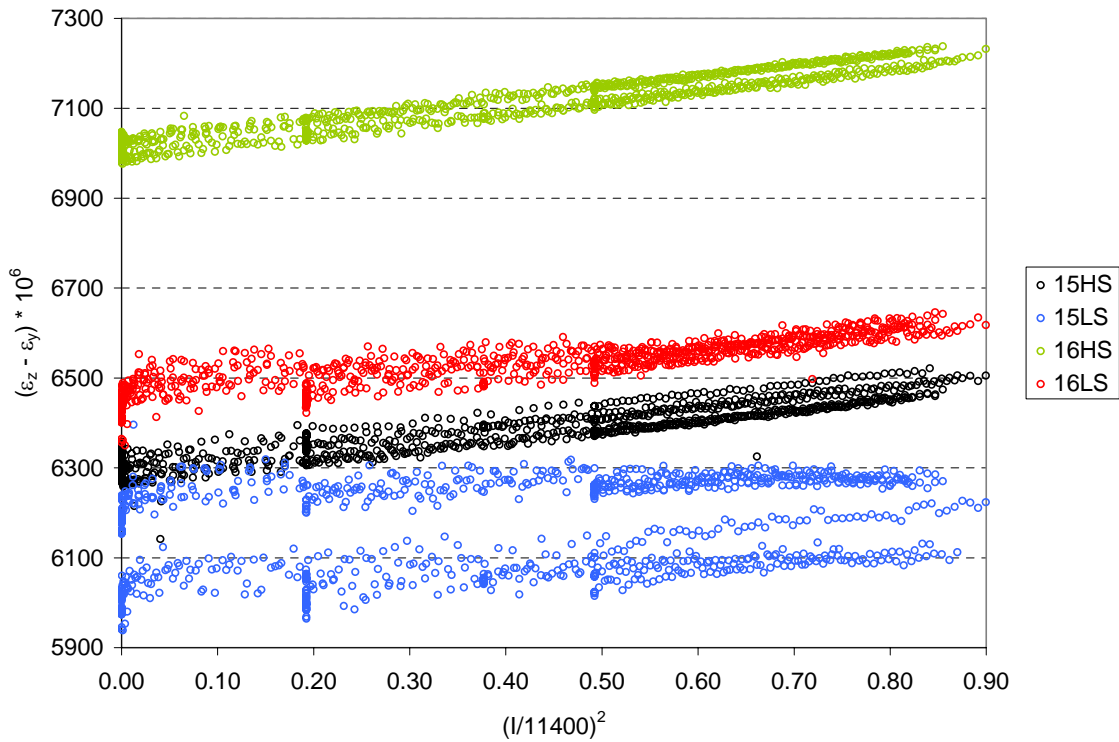


Fig. 55. Strain difference ($\cdot 10^6$) in the coil straight sections during magnet excitation as a function of the fraction of Lorentz force with respect to short sample.

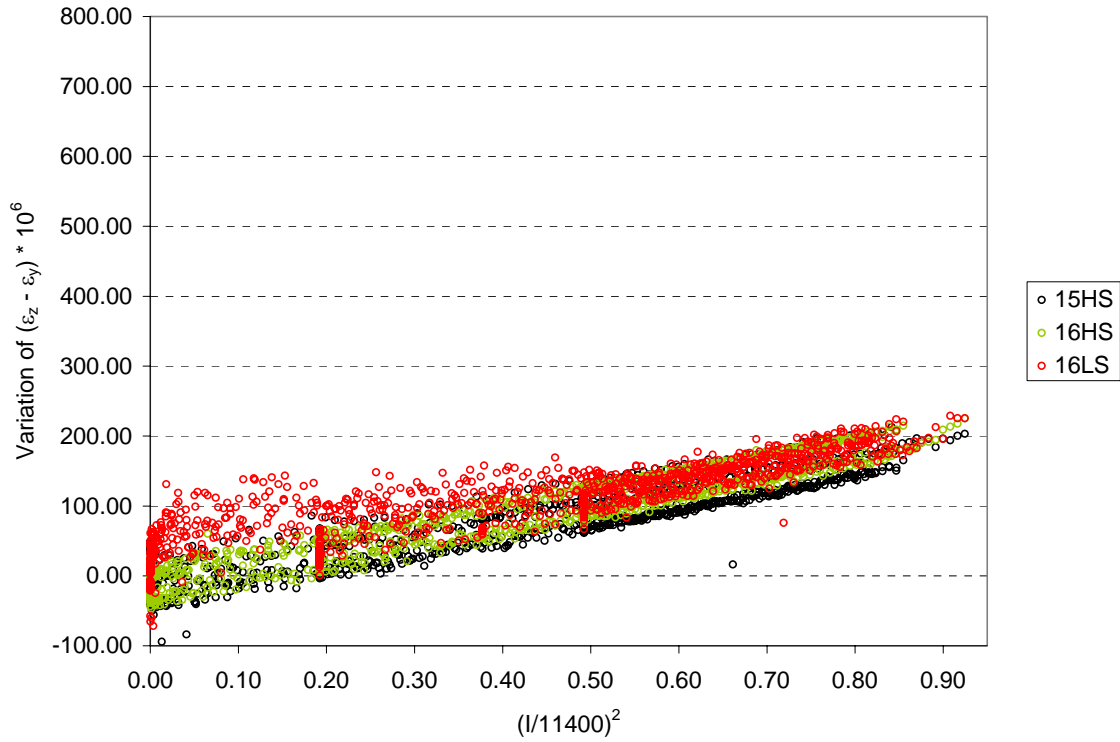


Fig. 56. Variation of strain difference ($\cdot 10^6$) in the coil straight sections during magnet excitation as a function of the fraction of Lorentz force with respect to short sample.

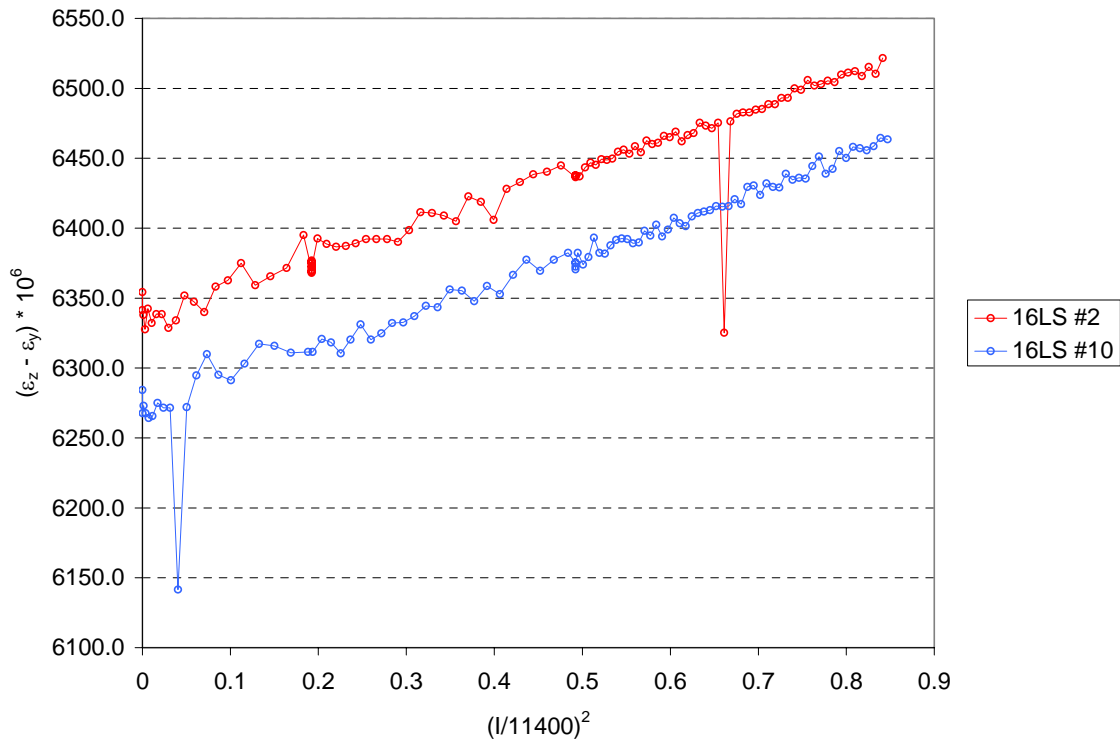


Fig. 57. Strain difference ($\cdot 10^6$) in the coil straight sections during magnet excitation as a function of the fraction of Lorentz force with respect to short sample: quench #2 and quench #10.

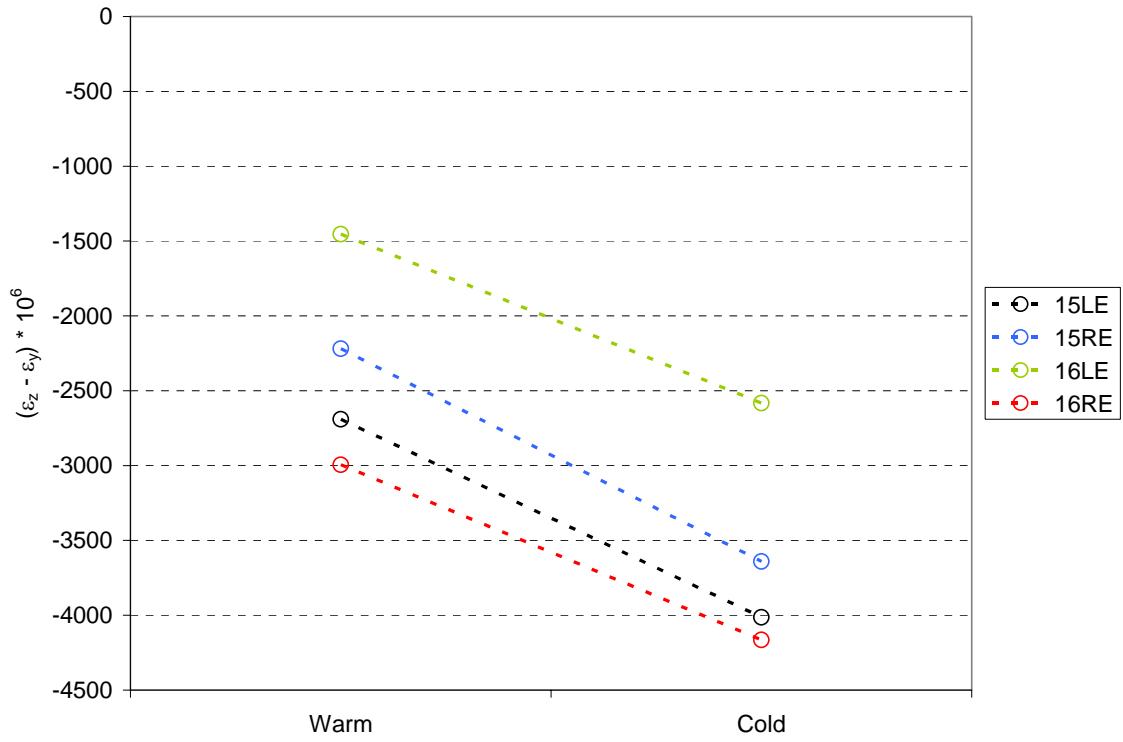


Fig. 58. Strain difference ($\cdot 10^6$) in the coil end regions during cool-down.

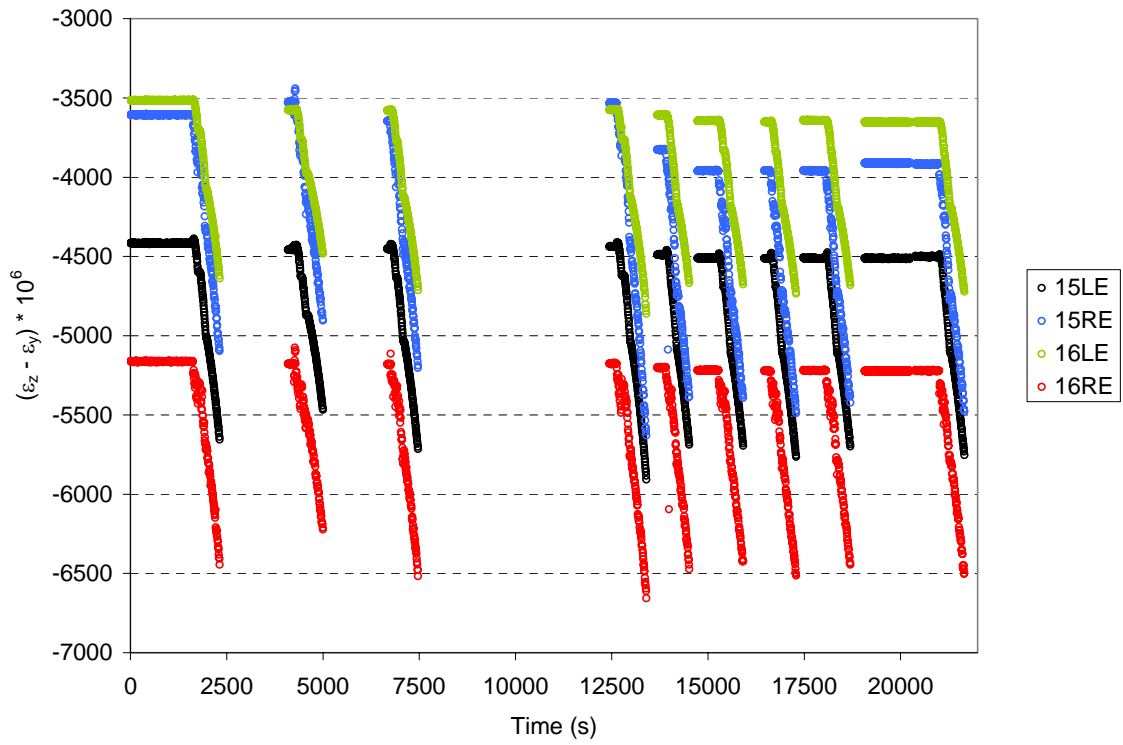


Fig. 59. Strain difference ($\cdot 10^6$) in the coil end regions during magnet excitation as a function of time (s).

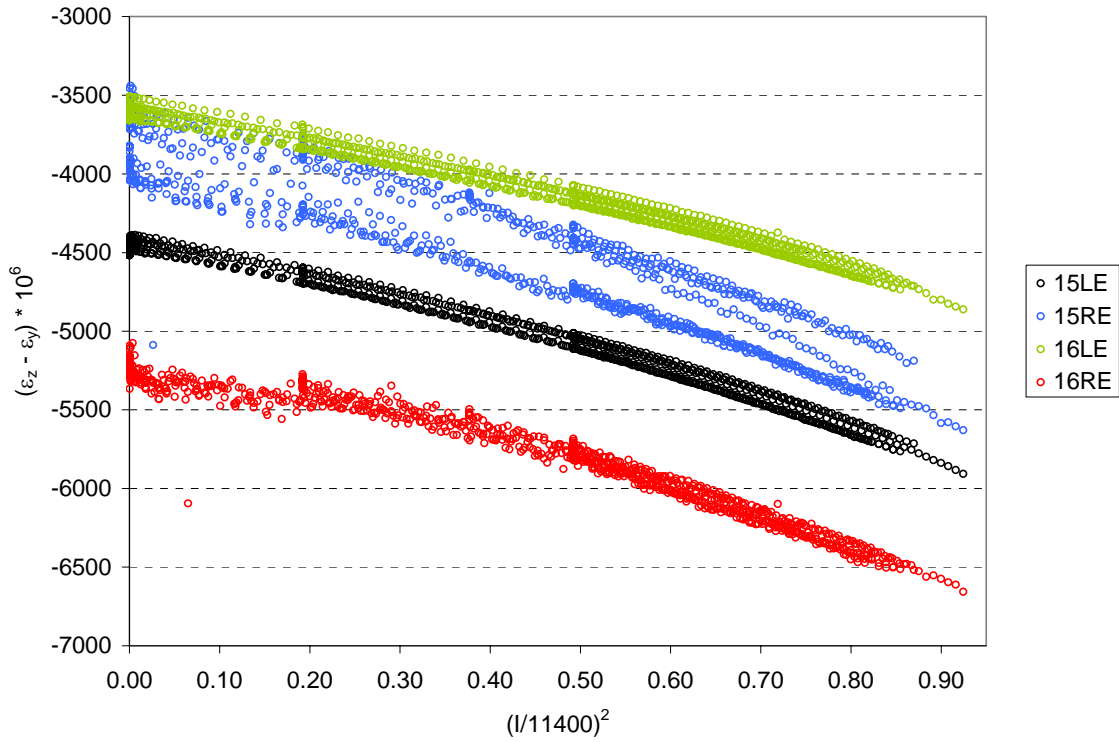


Fig. 60. Strain difference ($\times 10^6$) in the coil end regions during magnet excitation as a function of the fraction of Lorentz force with respect to short sample.

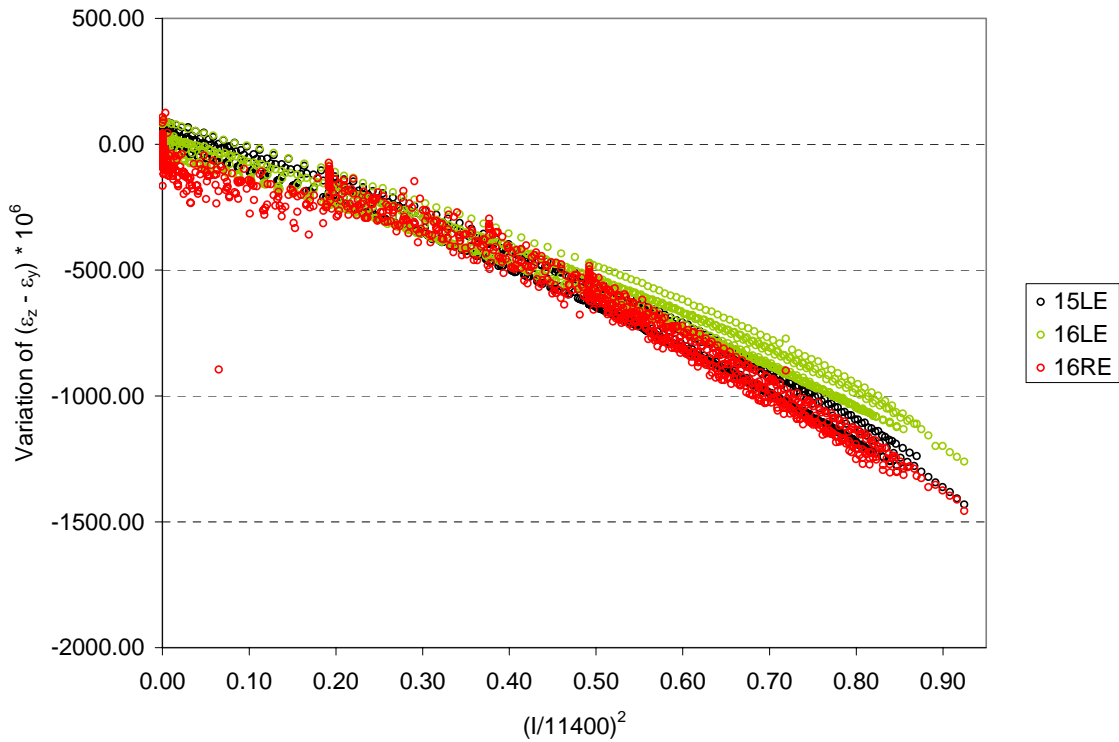


Fig. 61. Variation of strain difference ($\times 10^6$) in the coil end regions during magnet excitation as a function of the fraction of Lorentz force with respect to short sample.

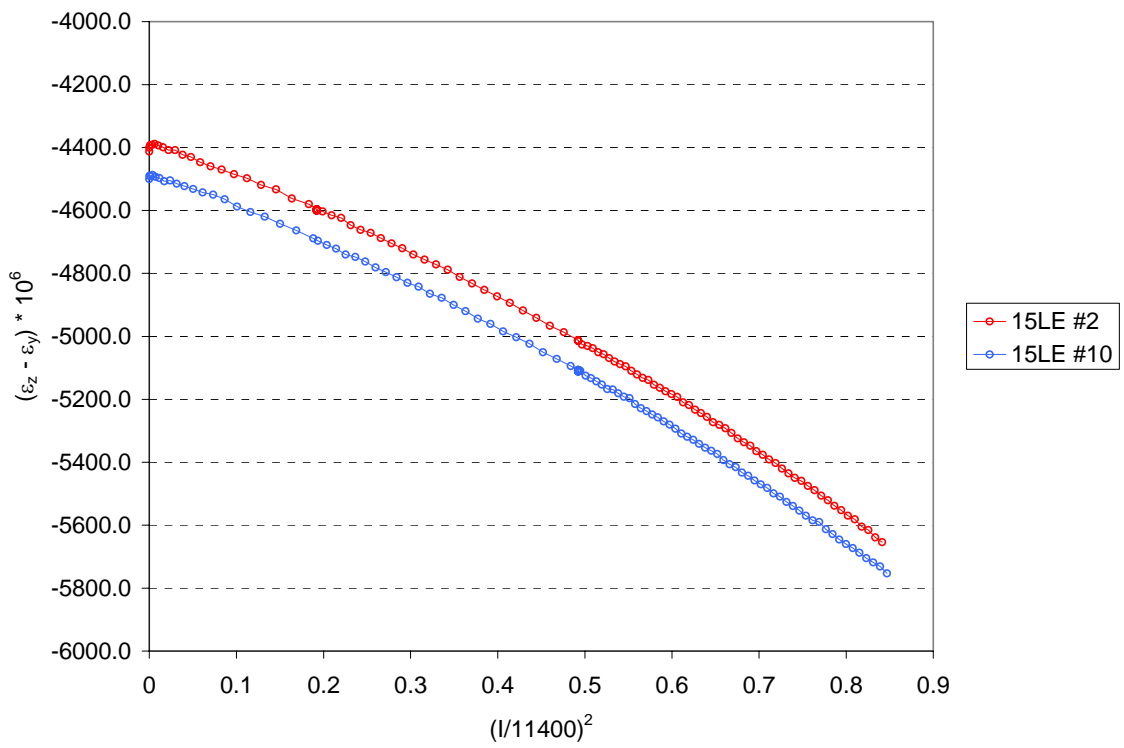


Fig. 62. Strain difference ($*10^6$) in the coil end regions during magnet excitation as a function of the fraction of Lorentz force with respect to short sample: quench #2 and quench #10.